

# Turbulent shear layers in a uniformly stratified background: DNS at high Reynolds number

Alexandra VanDine<sup>1</sup>, Hieu T. Pham<sup>1</sup> and Sutanu Sarkar<sup>1,2,†</sup>

<sup>1</sup>Department of Mechanical and Aerospace Engineering, University of California, San Diego, La Jolla, CA 92093, USA

<sup>2</sup>Scripps Institution of Oceanography, University of California San Diego, La Jolla, CA 92037, USA

(Received 20 July 2020; revised 22 January 2021; accepted 1 March 2021)

Direct numerical simulations are performed to investigate a stratified shear layer at high Reynolds number ( $Re$ ) in a study where the Richardson number ( $Ri$ ) is varied among cases. Unlike previous work on a two-layer configuration in which the shear layer resides between two layers with constant density, an unbounded fluid with uniform stratification is considered here. The evolution of the shear layer includes a primary Kelvin–Helmholtz shear instability followed by a wide range of secondary shear and convective instabilities, similar to the two-layer configuration. During transition to turbulence, the shear layers at low  $Ri$  exhibit a period of thickness contraction (not observed at lower  $Re$ ) when the momentum and buoyancy fluxes are counter-gradient. The behaviour in the turbulent regime is significantly different from the case with a two-layer density profile. The transition layers, which are zones with elevated shear and stratification that form at the shear-layer edges, are stronger and also able to support a significant internal wave flux. After the shear layer becomes turbulent, mixing in the transition layers is shown to be more efficient than that which develops in the centre of the shear layer. Overall, the cumulative mixing efficiency ( $E^C$ ) is larger than the often assumed value of  $1/6$ . Also,  $E^C$  is found to be smaller than that in the two-layer configuration at moderate  $Ri$ . It is relatively less sensitive to background stratification, exhibiting little variation for  $0.08 \leq Ri \leq 0.2$ . The dependence of mixing efficiency on buoyancy Reynolds number during the turbulence phase is qualitatively similar to homogeneous sheared turbulence.

**Key words:** stratified flows, stratified turbulence

## 1. Introduction

Turbulent mixing in the environment is a combination of both shear-driven and buoyancy-driven processes. In flows with a stable density gradient, buoyancy tends to

† Email address for correspondence: [ssarkar@ucsd.edu](mailto:ssarkar@ucsd.edu)

inhibit shear instabilities and shear-driven turbulence. Quantifying the rate of mixing has important implications in large-scale ocean and atmospheric models. Field observations and general circulation models rely heavily on the parametrization of mixing efficiency ( $E$ ) to quantify or prescribe the effect of turbulence, where  $E$  is understood to be the ratio of the gain in the background potential energy over the sum of the gain plus the dissipation rate of turbulent kinetic energy. For example, some ocean observations use  $E$  to estimate turbulent diffusivity ( $K_\rho$ ) and thereby vertical heat flux, while ocean models use  $E$  for subgrid turbulence closure (Jayne 2009; Whalen *et al.* 2015; Gregg *et al.* 2018). An accurate description of  $E$  is key in data interpretation and model prediction and the present study aims to improve our existing understanding of the mixing processes in stratified shear flows in nature and engineering.

One popular model is that suggested in Osborn (1980) in which the turbulent diffusivity is simply parameterized as  $K_\rho = \Gamma \kappa Re_b$ , where  $\kappa$  is the molecular diffusivity,  $\Gamma = E/(1 - E)$  is the flux coefficient (similar to the flux Richardson number) and  $Re_b = \varepsilon/\nu N^2$  is the buoyancy Reynolds number defined using the turbulent dissipation rate ( $\varepsilon$ ) and the squared buoyancy frequency ( $N^2$ ). Here, Osborn's formula is interpreted in the context of irreversible mixing (Ivey & Imberger 1991; Venayagamoorthy & Koseff 2016). Osborn (1980) suggested an upper-bound value of 0.2 for  $\Gamma$ . The validity of Osborn's model and, more specifically, the question of whether  $\Gamma$  has a fixed value, have received much attention. It has been shown that the flux coefficient  $\Gamma$  varies with Prandtl number ( $Pr$ ), buoyancy Reynolds number, turbulent Froude number ( $Fr = \varepsilon/NK$  where  $K$  denotes turbulent kinetic energy) and Richardson number ( $Ri$ ) (Strang & Fernando 2001; Shih *et al.* 2005; Mater & Venayagamoorthy 2014; Salehipour & Peltier 2015; Maffioli, Brethouwer & Lindborg 2016; Venayagamoorthy & Koseff 2016).

For homogeneous stratified shear turbulence in which shear and stratification are uniform over a turbulent region, Shih *et al.* (2005) proposed three regimes of mixing: a diffusive regime in which  $K_\rho = \kappa$  for  $Re_b < 7$ , an intermediate regime in which  $K_\rho = 0.2\nu Re_b$  for  $7 < Re_b < 10^2$  (similar to Osborn's model) and an energetic regime where  $K_\rho = 2\nu Re_b^{1/2}$  for  $Re_b > 10^2$ . In contrast, Portwood, de Bruyn Kops & Caulfield (2019) argued that the flux coefficient  $\Gamma$  does not vary over a wide range of  $Re_b$  and the regimes seen in Shih *et al.* (2005) are possibly due to transient effects. Salehipour *et al.* (2016) and Mashayek *et al.* (2017b) proposed two regimes for turbulence in a mixing layer with a two-layer density profile: a buoyancy-dominated regime in which  $K_\rho \propto Re_b^{3/2}$  for  $Re_b < Re_b^*$  and a shear-dominated regime where  $K_\rho \propto Re_b^{1/2}$  for  $Re_b > Re_b^*$ , where  $Re_b^* \approx 100\text{--}300$  is the buoyancy Reynolds number at which the mixing efficiency is at its maximum. Stratification in the natural environment is ubiquitous. It is presently unknown how mixing physics in such an environment, where the mixing layer is exposed to a uniform stratification outside the sheared zone, differs from the canonical problems of homogeneous stratified shear flow and two constant-density layers.

In the past two decades there has been a sustained effort to more accurately quantify mixing using three-dimensional, turbulence-resolving direct numerical simulations (DNS). Smyth & Moum (2000) and Caulfield & Peltier (2000) performed some of the first DNS of three-dimensional turbulence in a stratified shear layer to address the importance of shear-driven mixing. Since then, due to the benefits of increased computational power, DNS have been able to examine the rate of mixing at higher Reynolds numbers, most notably in the recent work by Mashayek & Peltier (2013), Salehipour, Peltier & Mashayek (2015), Salehipour & Peltier (2015) and Kaminski, Caulfield & Taylor (2017). Some significant results regarding  $\Gamma$  from these simulations are: (1)  $\Gamma$  has a significantly

higher value than 0.2, (2)  $\Gamma$  peaks at an intermediate value of stratification where secondary shear instabilities are the richest, and (3) the value of  $\Gamma$  varies significantly with Reynolds number, Prandtl number, Richardson number and even the amount of pre-existing turbulence in the shear layer (Brucker & Sarkar 2007; Kaminski & Smyth 2019).

Nearly all DNS of stratified layers at high Reynolds numbers use a hyperbolic tangent profile for both velocity and density in order to represent a shear layer that develops between two layers having different but constant density. In the oceans and atmosphere, it is typical that the stratification extends beyond the region of shear such that a spatially extensive stratification is a more appropriate representation of the density gradient than the spatially compact stratification of the two-layer profile. We are therefore motivated to simulate the evolution of a shear layer in fluid with space-filling uniform stratification.

There are intrinsic differences between these two configurations. First, the profiles of shear and stratification evolve similarly during the evolution of shear instabilities in the two-layer configuration since both have similar initial hyperbolic tangent profiles. However, stratification can evolve differently from shear in a uniformly stratified fluid. For the same value of  $Ri$  at the centre of the shear layer, the density difference across the layer is larger in the case with uniform stratification. In other words, the average value of the stratification is larger, leading to differences in the evolution of turbulence. Furthermore, ambient stratification, when sufficiently strong, can support propagating internal waves that transport momentum and energy into the far field. For example, in the problem of a moderately stratified shear layer adjacent to a pycnocline where the pycnocline  $N$  was varied in a DNS study, Pham, Sarkar & Brucker (2009) show that far-field internal waves are supported for a sufficiently large value of pycnocline  $N$ . At low  $Re = 1280$  the internal wave flux is shown to be as large as 17% of the turbulent production generated in the shear layer. The wave flux reduces as  $Re$  increases to 5000 (Pham & Sarkar 2010). Recent DNS of shear layers with uniform stratification in Watanabe *et al.* (2018) at  $Re = 6000$  reveal interesting turbulent dynamics at the turbulent/non-turbulent interface (TNTI). The authors also found that at low  $Ri$ , although internal waves do not propagate far from the shear layer, the wave flux measured at the TNTI can be comparable to the dissipation generated inside the shear layer. The DNS of Fritts *et al.* (2014) at a Reynolds number up to 10 000 indicate the development of secondary instabilities during the transition to turbulence, some of which are similar to those observed in the DNS with a two-layer density profile in Mashayek & Peltier (2013). However, it is unclear whether the secondary instabilities in Fritts *et al.* (2014) would enhance mixing efficiency. The effect of ambient stratification (external to the sheared zone) on the mixing rate is yet to be studied at high Reynolds number.

The present study seeks to investigate stratified turbulence and mixing at high Reynolds number in a shear layer with spatially compact shear using a density profile of space-filling, constant stratification. In addition to studying the route to turbulence and diagnostics of mixing, the present results are compared with the mixing parameterizations proposed by Shih *et al.* (2005), Salehipour *et al.* (2016), Mashayek *et al.* (2017b) and Osborn (1980). We address the following questions. (1) How does the evolution of the turbulent shear layer with uniform stratification differ from the two-layer configuration at high  $Re$ ? (2) Does the effect of uniform stratification enhance or reduce the mixing efficiency with respect to that which has been observed in prior studies of homogeneous stratified shear turbulence or mixing layer simulations with a two-layer density profile?

Besides the mixing efficiency in stratified shear flows, the present study also focuses on the dynamics of the transition layer (TL) which develops at the edges of the shear layer

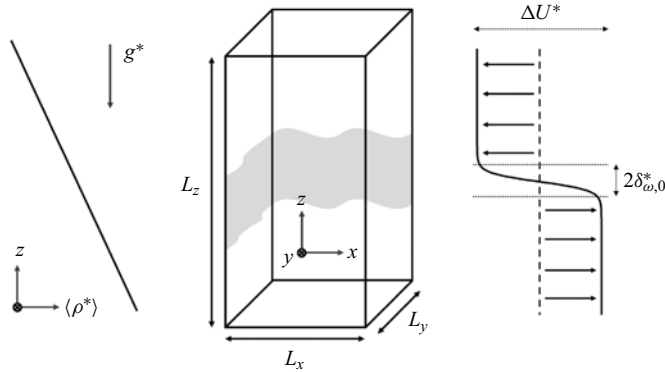


Figure 1. Sketch of the stratified shear layer with constant stratification.

during transition to fully three-dimensional turbulence. Previous simulations have shown TL with enhanced shear and stratification in the shear layer with uniform stratification (Pham *et al.* 2009; Watanabe *et al.* 2018). Simulations of the two-layer configuration also show formation of a TL although the enhancement of shear and stratification is significantly weaker (Mashayek & Peltier 2013). How the uniform stratification of the ambient can impact the development of the TL as well as the turbulence and mixing therein remains to be answered. Furthermore, the implications of the TL to mixing parameterizations requires thorough investigation.

This work is organized as follows. In § 2 the initialization and numerical formulation of the stratified shear layer is introduced. Section 3 provides a discussion of the evolution of the shear layer with specific emphasis on instabilities and subsequent turbulence. The structure of the TL, its turbulence and the wave flux across it are examined in § 4. A discussion of the mixing efficiency and its parameterization follows in § 5. The findings are discussed in § 6 and conclusions are drawn.

## 2. Formulation

### 2.1. Stratified shear layer

The problem of a temporally evolving stratified shear layer with uniform stratification is considered. A sketch of the shear layer with relevant initialization parameters is shown in figure 1. The flow is constructed with a streamwise velocity field given by

$$\langle u^* \rangle(z^*, t = 0) = -\frac{\Delta U^*}{2} \tanh\left(\frac{2z^*}{\delta_{\omega,0}^*}\right), \quad (2.1)$$

where  $\Delta U^*$  denotes the velocity difference across the shear layer and  $\delta_{\omega,0}^* = \Delta U^*/(d\langle u^* \rangle/dz^*)_{max}$  is the initial vorticity thickness. Note that a superscript  $*$  denotes a dimensional quantity while the  $\langle \cdot \rangle$  operator indicates horizontal averaging.

Motivated by atmospheric and ocean observations in which stratification extends beyond regions of shear (Fritts 1982; Smyth, Moum & Caldwell 2001), this work utilizes a spatially extensive stratification. The density profile is initialized by a time-invariant uniformly stratified background density profile ( $\rho_b^*$ ). The background buoyancy frequency of the ambient fluid ( $N_0^{*2}$ ) has a constant value given by  $N_0^{*2} = -(g^*/\rho_0^*) d\rho_b^*/dz^*$ , where  $g^*$  is gravity and  $\rho_0^*$  is a reference density.

$Ri$	$L_x$	$L_y$	$L_z$	$L_{z,sl}$	$N_x$	$N_y$	$N_z$	$\Delta(\times 10^{-3})$	$\Delta/\eta_{min}$	$k_0$	$\delta_{TL}$
0.04	12.96	6.48	32.32	$-3 \leq z \leq 3$	2304	1152	1408	5.62	2.2	0.97	0.84
0.08	11.86	5.93	32.18	$-2 \leq z \leq 2$	2048	1024	1024	5.79	2.0	1.06	0.81
0.12	11.12	5.56	32.18	$-2 \leq z \leq 2$	1920	960	1024	5.79	1.9	1.13	0.69
0.16	10.13	5.07	32.5	$-2 \leq z \leq 2$	1792	896	1024	5.65	1.9	1.24	0.59
0.2	9.52	4.76	32.5	$-2 \leq z \leq 2$	1536	768	1024	6.18	1.8	1.32	0.38

Table 1. Parameters used to construct the computational domain: domain length ( $L_x, L_y, L_z$ ), region with uniform grid spacing in the vertical direction ( $L_{z,sl}$ ), number of grid points ( $N_x, N_y, N_z$ ), grid spacing in the shear layer ( $\Delta$ ), grid spacing normalized by the smallest Kolmogorov length scale and peak wavenumber  $k_0$  of the energy spectrum used to generate the initial velocity perturbations. The thickness of the upper TL ( $\delta_{TL}$ ) at late time is given in the last column.

The governing equations for this problem are the three-dimensional Navier–Stokes equations for an unsteady, incompressible flow with the Boussinesq approximation. A Cartesian frame of reference is used to represent the streamwise, spanwise and vertical coordinates such that spatial orientation and velocities are given by  $x_i = (x, y, z)$  and  $u_i = (u, v, w)$ , respectively. The density equation is solved for the non-dimensional density deviation ( $\tilde{\rho}$ ) from the uniform background. Similarly, the pressure ( $p$ ), which denotes the deviation from the pressure which is in hydrostatic balance with the background density ( $\rho_b^*$ ), is solved for. The governing equations are non-dimensionalized using the following reference quantities: velocity difference ( $\Delta U^*$ ), initial vorticity thickness ( $\delta_{\omega,0}^*$ ) and a reference value for density deviation ( $\Delta\rho^* = \delta_{\omega,0}^* d\rho_b^*/dz^*$ ). The resulting non-dimensional equations are given by

$$\frac{\partial u_j}{\partial x_j} = 0, \tag{2.2a}$$

$$\frac{\partial u_i}{\partial t} + \frac{\partial(u_j u_i)}{\partial x_j} = -\frac{\partial p}{\partial x_i} + \frac{1}{Re} \frac{\partial^2 u_i}{\partial x_j \partial x_j} - Ri \tilde{\rho} g_i, \tag{2.2b}$$

$$\frac{\partial \tilde{\rho}}{\partial t} + \frac{\partial(u_j \tilde{\rho})}{\partial x_j} = \frac{1}{Re Pr} \frac{\partial^2 \tilde{\rho}}{\partial x_j \partial x_j} - w. \tag{2.2c}$$

Non-dimensional parameters, namely the initial Reynolds number ( $Re$ ), initial gradient Richardson number at the centre of the shear layer ( $Ri$ ) and Prandtl number ( $Pr$ ) are as follows:

$$Re = \frac{\Delta U^* \delta_{\omega,0}^*}{\nu^*}, \quad Ri = \frac{N_0^{*2} \delta_{\omega,0}^{*2}}{\Delta U^{*2}}, \quad Pr = \frac{\nu^*}{\kappa^*}. \tag{2.3a-c}$$

Here,  $\nu^*$  and  $\kappa^*$  are the kinematic viscosity and thermal diffusivity, respectively.

### 2.2. Numerical methods and simulation set-up

Five DNS cases are simulated as listed in table 1. All cases have  $Re = 24\,000$  and  $Pr = 1$  while the strength of stratification is varied such that  $Ri = [0.04, 0.08, 0.12, 0.16, 0.2]$  encompasses a wide range of background stability from weakly stratified at  $Ri = 0.04$  to strongly stratified at  $Ri = 0.2$ .

The numerical methods employed to solve the governing equations are similar to DNS of our previous work (Brucker & Sarkar 2007; Pham & Sarkar 2010; VanDine,

Chongsiripinyo & Sarkar 2018). The Williamson low-storage, third-order Runge–Kutta method is employed for time advancement while the discretization of spatial derivatives is achieved using a second-order, central finite difference scheme. The Poisson equation for pressure is solved using a parallel multigrid solver. The streamwise and spanwise directions have periodic boundary conditions. In the vertical direction, vertical velocity has a homogeneous Dirichlet boundary condition while homogeneous Neumann boundary conditions are enforced for horizontal velocity components, density deviation and pressure. In a sponge region near the vertical boundaries in the regions  $z > 10$  and  $z < -10$  (sufficiently far from the shear layer), a Rayleigh damping function gradually relaxes the density and velocities to their corresponding boundary values in order to damp propagating fluctuations and prevent reflections of features such as internal waves which have propagated far from the shear layer.

For this work, an isotropic grid is used in the central region of the shear layer with a grid spacing of  $\Delta x = \Delta y = \Delta z = \Delta$  as indicated in table 1. The streamwise and spanwise grids have uniform spacing while mild stretching is used in the vertical outside the shear layer. Throughout the entire grid, the grid spacing is less than  $2.2\eta$ , where  $\eta = (\nu^3/\varepsilon)^{1/4}$  ( $\varepsilon$  denotes turbulent kinetic energy dissipation rate) is the Kolmogorov length scale, thus indicating appropriate resolution for capturing small-scale fluctuations. The number of grid points in the streamwise, spanwise and vertical directions are given by  $(N_x, N_y, N_z)$  and the domain extent is given by  $(L_x, L_y, L_z)$  as denoted in table 1. The computational domain is large enough to accommodate two wavelengths of the most unstable Kelvin–Helmholtz (K–H) mode in the streamwise direction and one wavelength in the spanwise direction. The sufficiently large spanwise domain is required in order to accurately capture the transition from two-dimensional K–H shear instability to three-dimensional turbulence and also to ensure good convergence of statistics. The spanwise domain size is about two times and the number of grid points is about four times larger than in the cases of Mashayek, Caulfield & Peltier (2013) with the equivalent  $Re$ . Due to the different characteristic length and velocity scales used in the non-dimensionalization of the governing equations, the Reynolds number of 24 000 in the present study is equivalent to  $Re = 6000$  in Mashayek & Peltier (2013). We choose this value of  $Re$  since their results suggest the influence of secondary instabilities on the rate of mixing is most profound when  $Re$  is at or larger than this value.

The flow is initialized using velocity perturbations for which the broadband spectrum is given by  $E(k) \propto k^4 \exp[-2(k/k_0)^2]$ , where the peak value of  $E(k)$  is found at  $k_0$  (values given in table 1) corresponding to the fastest growing mode of the K–H instability. The root mean square (r.m.s.) of each velocity component has a peak of 0.1 %  $\Delta U$  at the centre of the shear layer. The following shape function,  $F(z) = \exp[-(z/\delta_{\omega,0})^2]$ , is used to confine the fluctuations to inside the shear layer.

### 2.3. Linear stability analysis of K–H shear instability

In order to construct the computational grid, linear stability analysis (LSA) is performed to search for the fastest growing normal mode of the K–H shear instability. Stability theory of a stratified shear layer with a two-layer hyperbolic density profile suggests a condition of  $Ri < 0.25$  for the shear instability to develop. The growth rate ( $\sigma$ ) of the fastest growing mode (FGM) is significantly reduced as  $Ri$  increases toward 0.25 in an analysis (Hazel 1972) which assumes that the fluid is inviscid and that the shear layer is located inside an infinite domain.

Here, the LSA is performed, taking into account the effect of viscosity, diffusivity and a finite domain, to examine the FGM when the shear layer is uniformly stratified. The theory and numerical implementation of the LSA is given in Smyth, Moum & Nash (2011). In the LSA, the Reynolds number, Prandtl number and domain size ( $L_z$ ) have the same values as in the DNS. The grid spacing is  $\Delta z = 0.025$ . Free-slip and fixed buoyancy conditions are used at the top and bottom boundaries. The LSA of the two-layer profile is also performed for comparison.

Figure 2(a,b) contrasts the mean profiles of the squared buoyancy frequency ( $N^2$ ), squared rate of shear ( $S^2$ ) and gradient Richardson number ( $Ri_g$ ) in the two-layer shear layer to those in the linearly stratified shear layer. The same level of stratification at the centre of the shear layer,  $N^2 = 0.12$ , is used. Away from the centre,  $N^2$  decreases to zero in the two-layer case while it remains constant in the other case. As a result,  $Ri_g$  in the two-layer case is smaller than that in the case with linear stratification throughout the shear layer except at the centre where  $Ri_g = 0.12$  in both cases. With the same amount of mean kinetic energy, e.g. the same velocity profile, the potential energy barrier inside the shear layer is significantly higher in the case with linear stratification, thereby reducing the growth rate of the K–H shear instability.

Results of the LSA are shown in figure 2(c,d). In the two-layer case, the growth rate ( $\sigma$ ) is similar to that of Hazel (1972) in the region with low  $k$  and  $Ri$ . However, as  $k$  and  $Ri$  increase, the growth rate becomes slightly smaller than the value from Hazel (1972) due to the effect of viscosity, diffusivity and a finite domain. The location of FGMs (marked by a white line) in  $k\delta_{\omega,0} - Ri$  space indicates a significant difference between the two configurations. While the wavenumber of the K–H modes varies little with  $Ri$  in the two-layer case, the K–H modes show a larger value of  $k$  and thus a shorter wavelength as  $Ri$  increases in the case with uniform stratification. Figure 2(e,f) contrasts the growth rate between the two cases for the five values of  $Ri$  used in the DNS to be discussed. At the same  $Ri$ , the growth rate of the K–H mode is higher in the two-layer case which suggests the K–H shear instability in the case with uniform stratification is weaker.

#### 2.4. Statistical analysis

The velocity, density and pressure fields are decomposed using Reynolds decomposition into mean (horizontal average) and fluctuating components denoted by  $\langle \rangle$  and  $'$ , respectively. In later discussions, the turbulent kinetic energy (TKE) budget will be used to examine the routes to turbulence and is given by

$$\frac{DK}{Dt} = P - \varepsilon + B - \frac{\partial T_3}{\partial z}, \tag{2.4}$$

with TKE ( $K$ ), production ( $P$ ), dissipation ( $\varepsilon$ ), buoyancy flux ( $B$ ) and the transport term ( $T_3$ ) specified as

$$\left. \begin{aligned} K &= \frac{1}{2} \left( \langle u' \rangle^2 + \langle v' \rangle^2 + \langle w' \rangle^2 \right), \\ P &= -\langle u'w' \rangle \frac{\partial \langle u \rangle}{\partial z}, \quad \varepsilon = \frac{2}{Re} \langle s'_{ij}s'_{ij} \rangle, \quad s'_{ij} = \frac{1}{2} \left( \frac{\partial u'_i}{\partial x_j} + \frac{\partial u'_j}{\partial x_i} \right), \\ B &= -Ri \langle \rho'w' \rangle, \quad T_3 = \frac{1}{2} \langle w'u'_i u'_i \rangle + \frac{1}{\rho_0} \langle w'p' \rangle - \frac{2}{Re} \langle u'_i s'_{3i} \rangle. \end{aligned} \right\} \tag{2.5}$$

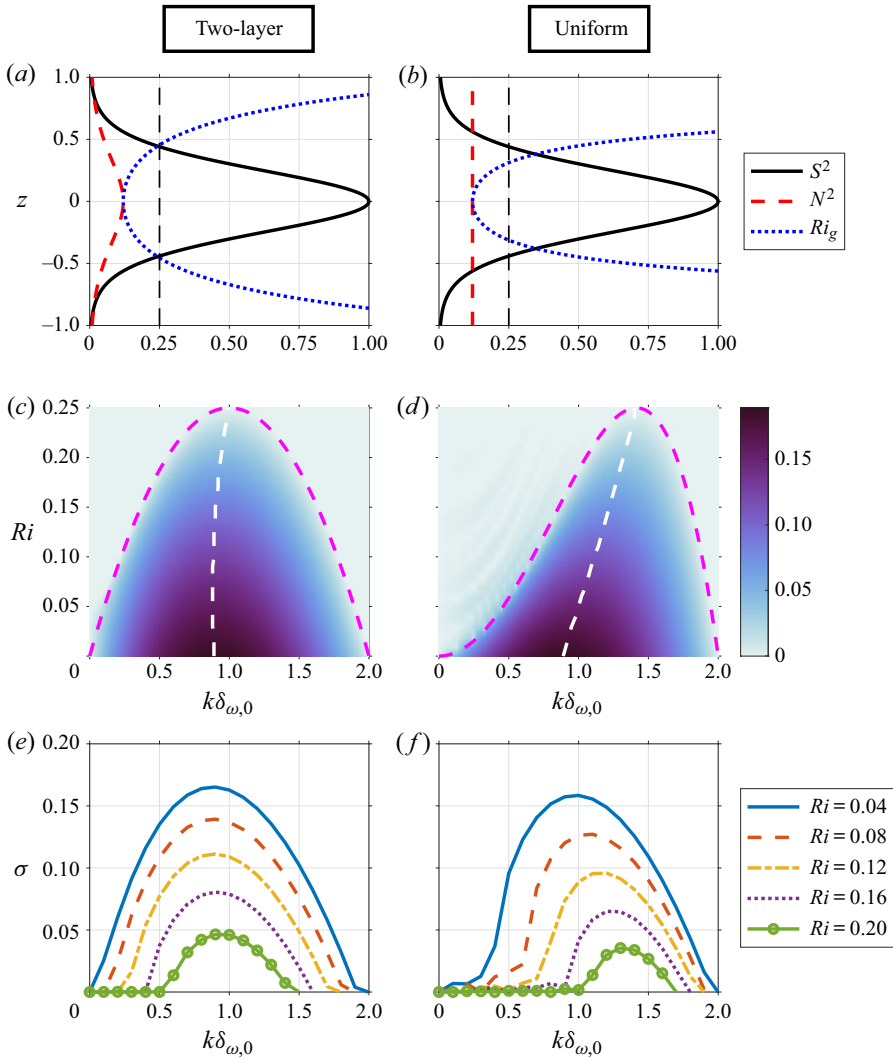


Figure 2. Effect of stratification on flow instability using LSA. Plots (a,c,e) correspond to the two-layer density profile and (b,d,f) to the linear density profile with uniform  $N^2$ . (a,b) Initial profiles of  $S^2$ ,  $N^2$  and  $Ri_g$ . (c,d) Contours of growth rate ( $\sigma$ ) as a function of  $Ri$  and wavenumber ( $k$ ). (e,f) Plots showing  $\sigma(k)$  in the five simulated  $Ri$  cases. Dashed magenta lines in (c,d) mark the stability boundary,  $Ri = k(1/2 - k/4)$  (Hazel 1972) and  $Ri = k^2(1/4 - k^2/16)$  (Drazin 1958), respectively. Solid white lines in (c,d) indicate the location of the FGMs of the K–H instability.

In order to calculate mixing efficiency, numerous studies have used a method which quantifies available and background potential energy by sorting the density field (Winters *et al.* 1995). This method produces a bulk value of the mixing efficiency which is representative of the entire shear layer. Instead, we use the dissipation of the density field as a surrogate to the change in background potential energy such that the mixing efficiency ( $E$ ) is given by

$$E = \frac{\varepsilon_\rho}{\varepsilon + \varepsilon_\rho}, \quad \varepsilon_\rho = \frac{1}{Re Pr} \frac{g^2}{\rho_0^2 N_0^2} \left\langle \frac{\partial \rho'}{\partial x_i} \frac{\partial \rho'}{\partial x_i} \right\rangle, \quad (2.6a,b)$$

where  $\varepsilon_\rho$  is the dissipation rate of turbulent available potential energy (TAPE =  $g^2 \langle \rho'^2 \rangle / 2\rho_0^2 N_0^2$ ). Scotti & White (2014) have demonstrated that this method of computing the mixing efficiency produces accurate results for turbulence in a continuously stratified fluid. Furthermore, this method is able to provide the spatial variability of the mixing efficiency throughout the shear layer as opposed to a single bulk value.

### 3. Flow evolution

#### 3.1. Routes to turbulence: K–H shear instability and secondary instabilities

In a shear layer with inflectional shear it is understood that there is a strong primary instability in the form of a K–H shear instability. This instability manifests as a series of vortices which roll up over time (termed billows) and are connected by vorticity filaments (termed braids). As the K–H billows evolve, secondary instabilities develop throughout the shear layer (Mashayek & Peltier 2012*a,b*; Thorpe 2012; Arratia, Caulfield & Chomaz 2013; Salehipour *et al.* 2015). In the following discussion we use the visualization of density and vorticity fields to illustrate that, as in the shear layer between two layers of constant density, the continuously stratified shear layer exhibits rich dynamics of secondary instabilities. In the present study we do not perform LSA for each type of instability since they are already discussed in depth in previous studies. Instead, we focus on the effect of the continuous stratification and the resulting mixing driven by the secondary instabilities. Our identification of secondary instabilities is based on visual inspection and comparison with previous work in the two-layer problem. It is also noted that pairing of K–H billows is not found at the high  $Re$  of the present study. At sufficiently high  $Re$ , secondary instabilities break down the billows before their co-rotation and pairing as was found by Pham & Sarkar (2010) when  $Re$  was increased to 5000 relative to their earlier work at  $Re = 1280$ .

The  $Ri = 0.04$  case is used to outline the general development of the stratified shear layer, and differences between the various  $Ri$  cases are discussed thereafter. Figure 3 shows cross-sectional snapshots of the density ( $\rho$ ) and spanwise vorticity ( $\omega_2 = \partial u / \partial z - \partial w / \partial x$ ). Specific snapshots in time are shown where the time ( $t$ ) represents the non-dimensional time,  $S_0^* t^*$ , where  $S_0^*$  is the initial centreline shear. The primary shear instability is evident in figure 3(a) in the form of two K–H billows. As the billows grow vertically, they extract kinetic energy from the shear layer. Once they reach the maximum vertical extent, the K–H billows spread in the streamwise direction and deform into elliptical shape similar to the observation by Arratia (2011). A spanwise variability also develops early to further disrupt the flow as indicated in the spanwise snapshots of  $\rho$  and  $\omega$  in figure 3(a). The billow continues to develop horizontal motions and r.m.s. spanwise velocity fluctuations (not shown) increase in this case. Note that there is no broadband turbulence as yet in the development. As small-scale fluctuations are allowed to develop due to low viscosity (high  $Re$ ), the billows begin to break down by secondary instabilities. A counter-rotating vortex pair denoting secondary convective instability (SCI) is seen at  $(x, z) \approx (7, 0)$  in the streamwise snapshot of  $\omega_2$  in figure 3(b). Multiple occurrences of SCI develop in the eyelids of the two billows. The spanwise snapshot of  $\omega_2$  suggests the SCI is highly three dimensional unlike the two-dimensional K–H billows with little spanwise variability seen at the earlier time. Strong vortices which develop in the centre of the billow cores at  $(x, z) \approx (3, 0)$  and  $(8, 0)$  also contribute towards transition to turbulence. In the DNS with uniform stratification at  $Re = 10\,000$  and  $Ri = 0.05$ , Fritts *et al.* (2014) observed that secondary instabilities arise initially in the eyelid and the resulting turbulence spreads inward into the core. Here, we observe growth of SCI in the eyelids and strong vortices in the billow cores at the same time. Eventually, the breaking billows become localized

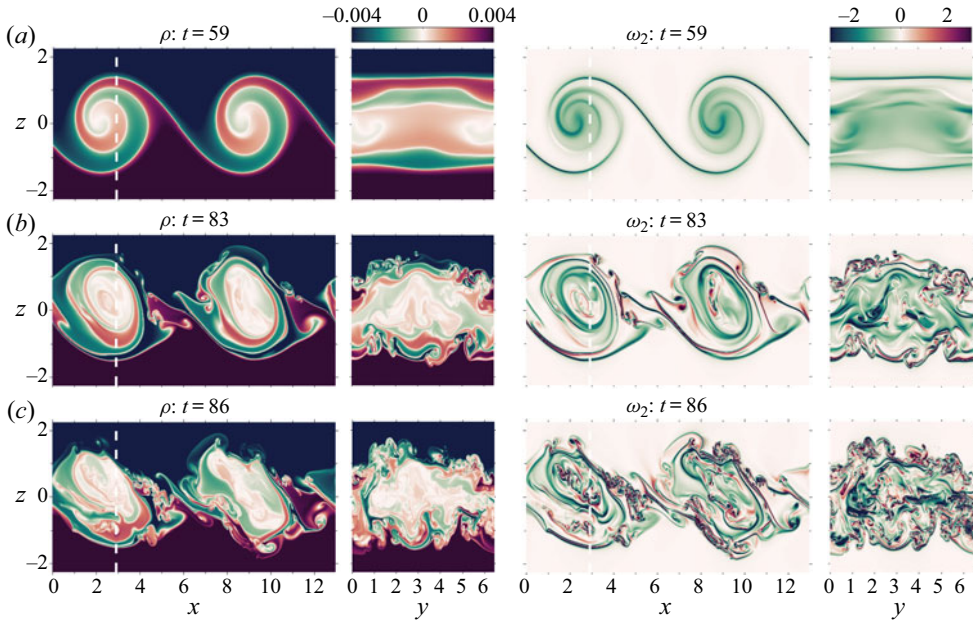


Figure 3. Cross-sectional snapshots of the density ( $\rho$ ) and spanwise vorticity ( $\omega_2$ ) fields for the  $Ri = 0.04$  case at (a)  $t = 59$ , (b)  $t = 83$  and (c)  $t = 86$ . From left to right, the columns show a streamwise cross-section of  $\rho$  at  $y = L_y/2$ , spanwise cross-section of  $\rho$  along the dotted line shown in the first column, streamwise cross-section of  $\omega_2$  at  $y = L_y/2$  and a spanwise cross-section of  $\omega_2$  along the dotted line shown in the third column. In this plot and henceforth,  $x$ ,  $y$  and  $z$  are noted to be the streamwise, spanwise and vertical coordinates, respectively, made non-dimensional using  $\delta_{\omega,0}$ .

patches of turbulence with the majority of overturning occurring at the core of each billow as shown in figure 3(c).

The flow evolves differently at moderate stratification ( $0.08 \leq Ri \leq 0.16$ ) with the K–H billows exhibiting smaller vertical growth followed by faster spreading in the streamwise direction and deformation into elliptical billows as illustrated in figure 4. Unlike the  $Ri = 0.04$  case in which the SCI initiates the transition to three-dimensional turbulence, the streamwise snapshots of  $\rho$  and  $\omega_2$  in figure 4(a) indicates the secondary shear instability (SSI) also contributes to the transition. The negative- $\omega_2$  vortices which grow along the braids in the regions  $1 < x < 2$  and  $9.5 < x < 10.5$  are indicative of SSI. As  $Ri$  increases, SSI overtakes SCI as the dominant mechanism that breaks down the K–H billows when contrasting figures 4(a) through 4(c). In  $Ri = 0.08$ – $0.16$  cases, vortices that grow at the top of the left billow are suggestive of secondary core deformation instability (SCDI). Mashayek & Peltier (2012b) found SCDI is associated with an observable inflation of the core. They also suggested that the growth rate of SCDI decreases with increasing  $Ri$ . The vortices that break down the left billow in figure 4(a–c) are also less energetic as  $Ri$  increases.

Beside SCI, SSI and SCDI, we also observe the development of localized core vortex instability (LCVI). When the core vortex bands grow and achieve a sufficiently large magnitude of  $\omega_2$ , LCVI form at the tips of the vorticity bands. The LCVI vortices and the bands from which they develop have spanwise vorticity with sign opposite to the background shear-layer vorticity (Mashayek & Peltier 2012b). The appearance of LCVI is particularly apparent at high  $Re$  because the K–H billows roll-up faster and there is less time for the vorticity bands in the core to diffuse. The streamwise snapshot of  $\omega_2$  shows

Turbulent shear layers in a uniformly stratified background

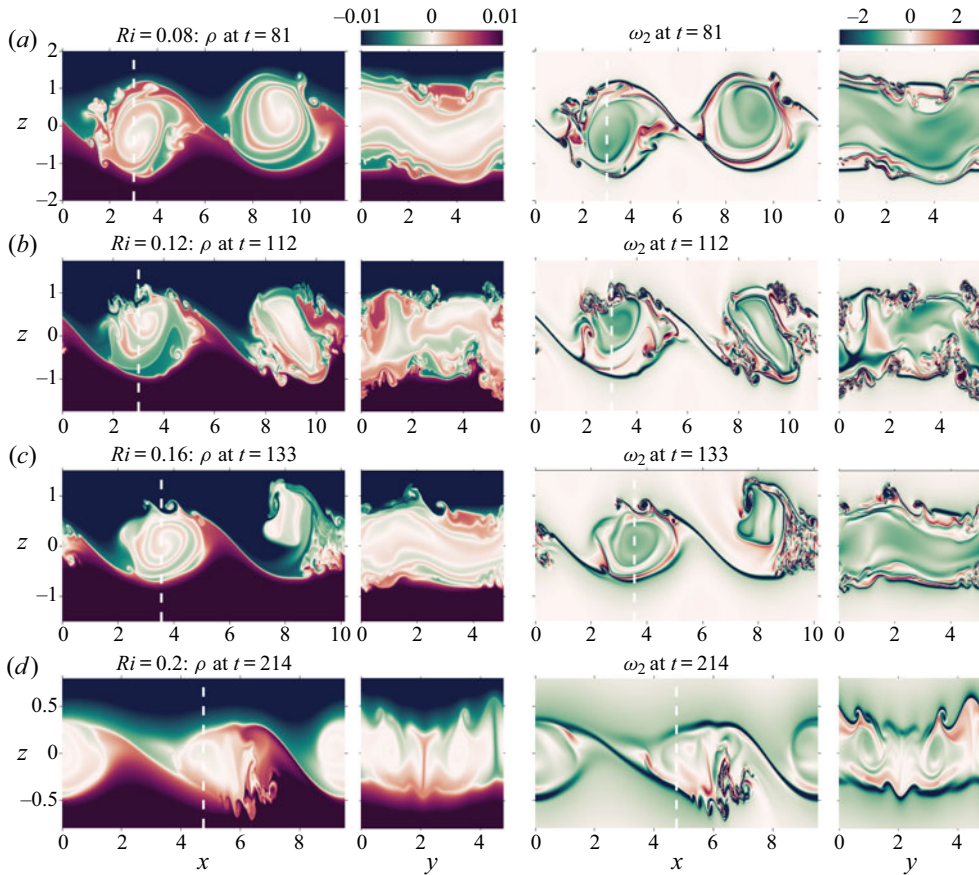


Figure 4. Cross-sectional snapshots of the density ( $\rho$ ) and spanwise vorticity ( $\omega_2$ ) fields for the four cases with  $Ri \geq 0.08$ . The column order is similar to figure 3: streamwise and spanwise cross-sections of  $\rho$  followed by streamwise and spanwise cross-sections of  $\omega_2$ . Note that the panels have differing aspect ratios and cover different ranges of  $x$  and  $z$  coordinates.

positive (red) vortices at  $(x, z) \approx (6, 0)$  and  $(7, 0)$  in figure 4(a). The two vortices develop from the tips of the negative (green) vortex bands in the eyelid indicating the growth of a LCVI.

At the high stratification of the  $Ri = 0.2$  case, the transition to turbulence is induced by SCDI and SCI. The multiple coherent vortices which develop in the lower half of the billow at  $(x, z) \approx (6, -0.5)$  in the streamwise snapshots of figure 4(d) are indicative of SCDI. The vertical strips of positive density at  $y = 2$  and negative density at  $y = 4.2$  in the spanwise snapshot are indicative of SCI. The strips resemble mushroom-like structures, a typical morphology of convective instabilities. We note the use of a large aspect ratio in figure 4(d) which distorts the mushroom-like structures into the vertical strips. While the mushroom-like structures in the  $Ri = 0.04$  case develop on the thin eyelid region of the K–H billows, the structures in this case with  $Ri = 0.2$  are significantly larger and they penetrate across the entire vertical extent of the billow. The DNS of Fritts *et al.* (2014) at the same  $Ri$  but with  $Re = 10\,000$  shows the prevalence of secondary instabilities in the billow cores. The absence of SCDI in their study is possibly due to a low Reynolds number effect.

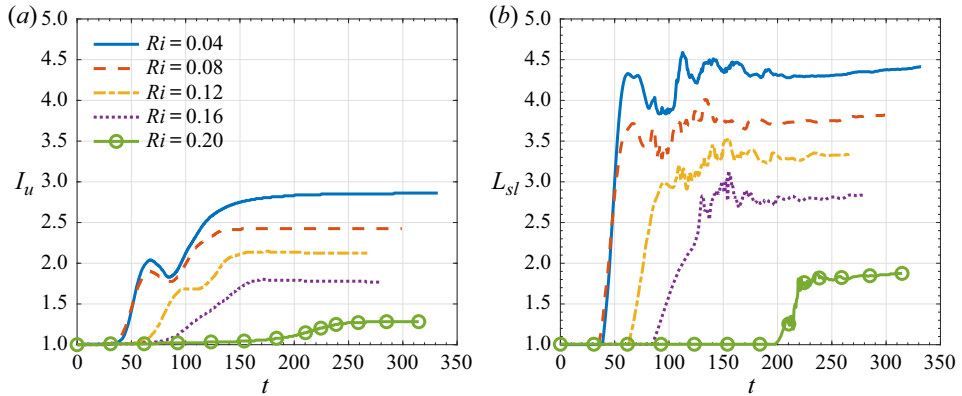


Figure 5. Temporal evolution of (a) momentum thickness ( $I_u$ ) and (b) shear-layer thickness ( $L_{sl}$ ) defined by the outer edges of the TL.

There are multiple modes that have similar vorticity manifestation such as the stagnation point instability (SPI) and secondary vortex band instability (SVBI). In fact, Mashayek & Peltier (2013) found that SVBI is a combination of both SPI and LCVI. Therefore, it is difficult to differentiate LCVI from SVBI without performing the stability analysis. Furthermore, the growth of secondary instabilities is highly sensitive to the initial broadband velocity fluctuations (Dong *et al.* 2019). We have simulated the  $Ri = 0.16$  case with two different choices for the initial velocity perturbations: one where the energy spectrum peaks at  $k_0 = 1.13$  and another with a peak at  $k_0 = 1.24$ . The horizontal domain length is chosen to accommodate two wavelengths of the most energetic mode in the initial velocity perturbations. While the evolution of the shear layer is statistically similar between the two cases, we find SPI to develop in only the former simulation with  $k_0 = 1.13$  and not the latter. The SPI manifests as a single vortex which develops at the stagnation point in the braid. Overall, with regard to the secondary instabilities, the transition to turbulence in the shear layer with uniform stratification is as dynamically rich as that observed in the case with a two-layer density profile. Readers should be aware that there are other secondary instabilities that have not been observed in either Mashayek & Peltier (2013) or the present study such as knot and tube instabilities (Thorpe 2012).

### 3.2. Effect of stratification on the growth of shear-layer thickness

The visualization of the evolving shear layer suggests that the thickness of the shear layer varies significantly with the stratification. Here, we quantify the thickness of the shear layer through two quantities: (1) the momentum thickness ( $I_u$ ) and (2) the layer bounded by the outer edges of the TLs denoted by  $L_{sl}$ . The first quantity provides an integral length scale which is used to compute non-dimensional numbers such as the bulk Richardson number, an important parameter typically used in the parameterization of shear-driven turbulence (Smyth & Moum 2000; Mashayek, Caulfield & Peltier 2017a). In contrast, the second quantity includes the mixing region at the edges of the shear layer. In the present study we identify the TL as a region with enhanced stratification (i.e.  $N^2/N_0^2 > 1$ ) formed at the edge of the shear layer due to vertical turbulent transport from the core of the shear layer to its edge. Figure 5 indicates a significant difference between the two quantities with  $L_{sl}$  up to 60% larger than  $I_u$  in the  $Ri = 0.16$  case at late time. In this section we focus the discussion on  $I_u$  and defer consideration of  $L_{sl}$  to the next section.

The momentum thickness, which is defined as

$$I_u = \int_{-10}^{10} [1 - 4 \langle u \rangle^2] dz \quad (3.1)$$

has the imprint of distinct flow regimes. At early time (approximately  $30 < t < 60$  in the  $Ri = 0.04$  and  $Ri = 0.08$  cases, and  $50 < t < 90$  in the  $Ri = 0.12$  case), the shear layer thickens rapidly due to the enlargement of the K–H billows. In all cases, except for the  $Ri \geq 0.16$  cases, there is a period where the shear layer briefly shrinks or stops growing before resuming its growth (approximately  $60 < t < 80$  in the  $Ri = 0.04$  and  $Ri = 0.08$  cases, and  $100 < t < 110$  in the  $Ri = 0.12$  case). At  $Ri = 0.12$ , the layer does not contract significantly as in the  $Ri = 0.04$  and  $Ri = 0.08$  cases but its growth pauses. The contraction of the shear layer persists longer at smaller  $Ri$  and is not seen at all in the  $Ri \geq 0.16$  cases indicating a key link of stratification to this flow feature. The period of contraction occurs during the transition from flow dominated by two-dimensional K–H rollers to fully three-dimensional turbulence. After its contraction or pause,  $I_u$  resumes growing before it asymptotes to a constant value at late time. At this time, buoyancy effects become sufficiently strong to cause turbulence decay and the shear layer can no longer thicken. Overall, the rate of growth decreases with increasing  $Ri$ . The ultimate thickness of the shear layer is also much smaller at higher  $Ri$ , e.g. barely 1.3 times its initial value in the  $Ri = 0.2$  case.

The contraction of the shear layer is linked to the energetics of turbulence. The momentum thickness, defined by (3.1), involves the mean kinetic energy (MKE) defined as  $\bar{K} = (\langle u \rangle^2)/2$ . Therefore, the change in momentum thickness is given by

$$\frac{dI_u}{dt} = \int_{-10}^{10} -8 \frac{\partial \bar{K}}{\partial t} dz. \quad (3.2)$$

From the Navier–Stokes equation, the evolution of MKE is governed by

$$\frac{D\bar{K}}{Dt} = -P - \bar{\varepsilon} - \frac{\partial \bar{T}_3}{\partial z}, \quad (3.3)$$

with viscous dissipation ( $\bar{\varepsilon}$ ) and the transport term ( $\bar{T}_3$ ) specified as

$$\bar{\varepsilon} = \frac{1}{Re} \left( \frac{\partial \langle u \rangle}{\partial z} \right)^2 \quad \text{and} \quad \bar{T}_3 = \langle u \rangle \langle u'w' \rangle - \frac{1}{Re} \langle u \rangle \frac{\partial \langle u \rangle}{\partial z}. \quad (3.4a,b)$$

The turbulent production ( $P$ ), which is defined previously in (2.4), acts as a transfer term between the MKE and TKE budgets. Equations (3.2) and (3.3) are combined to yield

$$\frac{dI_u}{dt} = \int_{-10}^{10} -8 \frac{\partial \bar{K}}{\partial t} dz \approx \int_{-10}^{10} 8P dz, \quad (3.5)$$

where the small contribution of the viscous dissipation of MKE inside the shear layer as well as the small transport term at  $z = \pm 10$  have been neglected. During the contraction of the shear layer when  $dI_u/dt < 0$ , MKE increases due to negative production as per (3.5).

Figure 6 illustrates the relationship between the MKE and  $P$  during the contraction period. As the K–H billows develop, they transport heavy fluid upward and light fluid downward which stirs the density gradient. Consequently, density increases in the upper half of the shear layer while it decreases in the lower half, as shown in figure 6(a). As the shear layer contracts, the denser fluid in the upper half of the shear layer is displaced

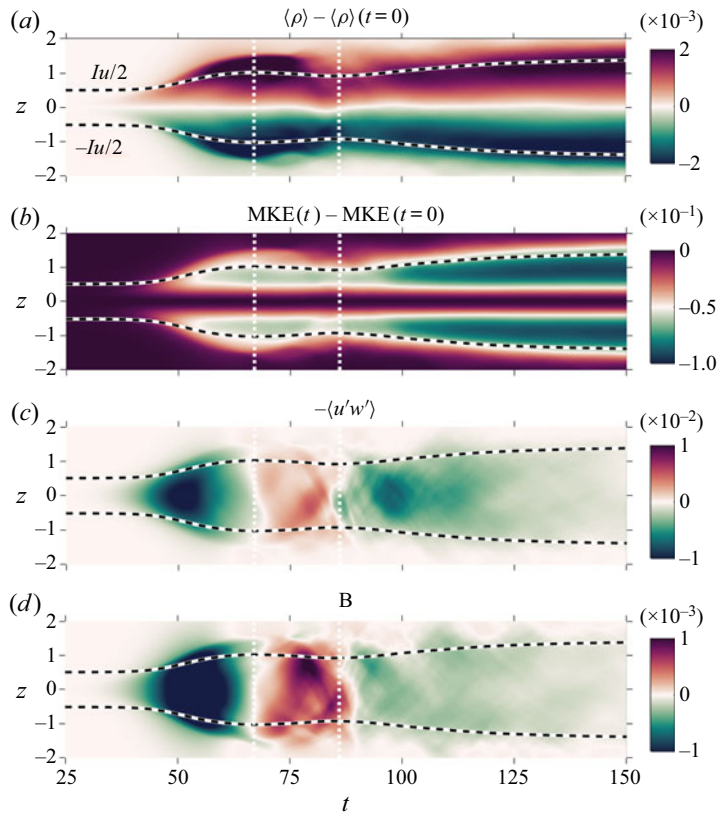


Figure 6. Evolution of the (a) density deviation from the initial profile, (b) MKE deviation from the initial profile, (c) momentum flux  $-\langle u'w' \rangle$  and (d) buoyancy flux  $B$  for the  $Ri = 0.04$  case. Dashed lines denote the boundaries of the shear layer defined as  $z = \pm I_u/2$ . Vertical dotted white lines mark the contraction period of the momentum thickness.

downward, releasing the available potential energy that was previously gained. During this period, the MKE shown in figure 6(b) increases notably at the edges of the shear layer ( $z = \pm 1$ ). At the time when the shear layer begins to contract marked by the first vertical dotted white line in figure 6(c), the momentum flux  $-\langle u'w' \rangle$  changes sign from negative to positive values signifying a counter-gradient momentum transport (CGMT). The CGMT occurs when the momentum flux does not follow the mean velocity gradient (Hussain 1986; Moser & Rogers 1993). Prior to the contraction, both the momentum flux and the mean velocity gradient have negative values, so the transport is down-gradient and the shear production is positive. In contrast, while the mean velocity gradient remains negative during the contraction, the momentum flux is counter-gradient and, thus, the negative production. After the contraction, the momentum transport reverts back to down-gradient and the production has positive values. Gerz & Schumann (1996) suggested that the energy of CGMT motions is provided by conversion of available potential energy to kinetic energy in homogenous stratified shear flows. Takamura *et al.* (2018) also found CGMT and negative production to occur in coherent vortices which develop during the transition from laminar to turbulent regimes in an unstratified mixing layer. It should be noted that contraction and CGMT were not observed in the DNS of a uniformly stratified shear layer at  $Re = 5000$  and  $Ri = 0.05$  (Pham & Sarkar 2010). It is interesting that the higher  $Re = 24\,000$  in the present study would enhance the CGMT.

*Turbulent shear layers in a uniformly stratified background*

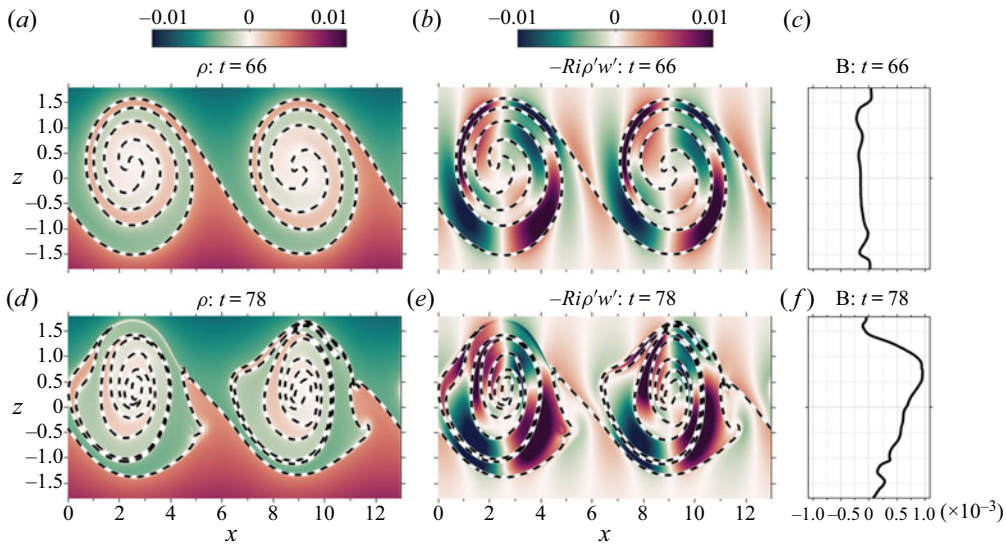


Figure 7. Cross-sectional snapshots of density ( $\rho$ ) and buoyancy flux  $-Ri\rho'w'$  fields as well as the profiles of horizontally averaged buoyancy flux ( $B$ ) in the  $Ri = 0.04$  case at two times: (a–c) before the contraction at  $t = 66$  and (d–f) during the contraction at  $t = 78$ . The  $x$ – $z$  planes are extracted at  $y = L_y/2$ . Dashed lines show the isopycnal contour of  $\rho = 0$ .

Komori & Nagata (1996) showed that CGMT in stratified flows is often accompanied by counter-gradient buoyancy flux (CGBF). We also observe CGBF during the contraction period as shown in figure 6(d). Prior to the contraction, the buoyancy flux ( $B$ ) is negative throughout the shear layer with a peak value locating at the centre of the shear layer. Once the shear layer contracts, the buoyancy flux switches sign from negative to positive values. The positive  $B$  concentrates near the edges of the shear layer with the centre of the layer having smaller positive values. The positive  $B$  supports the growth of SCI during the transition to turbulence. To better understand the roles of CGBF on the transition, figure 7 compares streamwise snapshots of the density and buoyancy flux before and during the contraction. As previously discussed, the primary K–H instability grows vertically until the potential energy barrier becomes too large, at which point, the billow contracts vertically and expands laterally in the streamwise direction. The deformation of the billows occurs coherently without inciting broadband turbulence. The change in vertical extent is clear between figures 7(a) and 7(d). Before the contraction at time  $t = 66$ , the instantaneous field of the buoyancy flux in figure 7(b) shows regions of both positive and negative values due to the stirring by the K–H billows. When averaged over the horizontal ( $x$ – $y$ ) plane, the net buoyancy flux ( $B$ ) has negative values as shown in figure 7(c). As the K–H billows deform during the contraction at time  $t = 78$ , the spatial distribution of the buoyancy flux changes significantly. The regions with positive values in the billows extend wider than that with negative values. As a result, the horizontal averaged values become positive as shown in figure 7(f). A wider area of positive buoyancy flux implies a higher tendency for SCI to grow. For example, the patch of positive buoyancy flux at  $(x, z) \approx (8, 0.5)$  in figure 7(e) induces the growth of the counter-rotating vortex pair at  $(x, z) \approx (7, 0)$  shown previously in figure 3(b). It is important to note that strong stratification inhibits CGMT and CGBF since the contraction does not occur in the  $Ri \geq 0.12$  cases. This is consistent with the finding of Mashayek & Peltier (2013)

who suggested the role of SCI becomes less important than SSI during the transition to turbulence at large  $Ri$ .

### 3.3. Effect of stratification on TKE budget and mixing efficiency

The evolution of depth-integrated terms in the TKE budget (figure 8) provides a comparison of turbulence energetics among the cases. The time for development of turbulence is substantially larger for the larger  $Ri$ , which is qualitatively consistent with the decrease of maximal growth rate with increasing  $Ri$ , shown previously in figure 2. The turbulent production  $P$  exhibits multiple peaks as time progresses, e.g. two distinct peaks in the cases with  $Ri \leq 0.12$ . When the stratification is weak as in the  $Ri = 0.04$  and  $Ri = 0.08$  cases, the integrated production (figure 8a) has significant negative values and the buoyancy flux (figure 8b) has significant positive values due to the CGMT and CGBF during the time interval of shear-layer contraction discussed in the previous section. It is after the contraction period that the shear layer becomes fully turbulent and the integrated  $\varepsilon$  in figure 8(c) increases sharply. The largest peak value of integrated  $\varepsilon$  occurs in the  $Ri = 0.04$  case, while the peak values are comparable in the three cases with  $0.08 \leq Ri \leq 0.16$ . The peak value decreases significantly in the  $Ri = 0.2$  case. Unlike the dissipation rate, the dissipation rate of the potential energy ( $\varepsilon_\rho$ ) in figure 8(d) develops earlier and during the contraction period. Noting that  $\varepsilon$  is insignificant during the contraction period, the flux coefficient has a high value (up to 0.7) during this period due to fine-scale coherent density structures inside the K–H billows. As previously shown, during the deformation of the K–H billows, density filaments/wisps inside the billows become significantly thinner. The filaments sharpen the density gradient in the shear layer down to the diffusive scale where it is dissipated by molecular diffusion. Interestingly, turbulence does not have a role in the mixing during this period despite the high Reynolds number. Furthermore, the peak values of  $\varepsilon_\rho$  are comparable among the  $Ri \leq 0.16$  cases unlike  $\varepsilon$ .

The cumulative (time- and space-integrated) TKE budget terms ( $P$ ,  $B$ , and  $\varepsilon$ ) and the dissipation rate ( $\varepsilon_\rho$ ) of the TAPE are shown in table 2. There is a large decrease of cumulative  $P$ , by approximately a factor of eight, with increasing  $Ri$ . The other quantities also decrease, but not proportionally, for instance,  $P/\varepsilon$  increases from the weakly stratified value of 1.5 to about 1.7 in the more stratified cases indicating that stratified shear-driven turbulence (under conditions which support its formation) is somewhat more dissipative than its neutral counterpart. The ratio of  $-B/\varepsilon$ , known as the flux Richardson number ( $Ri_f$ ), peaks in the  $Ri = 0.12$  case similar to the flux coefficient ( $\Gamma^C$ ). There is significant difference between reversible and irreversible mixing since  $Ri_f$  is substantially larger than  $\Gamma^C$ . The difference, which is approximately 27% in the  $Ri = 0.04$  case, decreases with increasing  $Ri$ .

We move to the mixing efficiency and examine its variation among the simulated cases. Figure 9(a) shows the cumulative mixing efficiency ( $E^C$ ), obtained by integrating  $\varepsilon_\rho$  and  $\varepsilon$  over the time duration of the simulations. The maximum value of  $E^C$  is approximately equal to 0.33 and occurs in the  $Ri = 0.12$  case. The  $Ri = 0.08$ , 0.16 and 0.2 cases have slightly smaller values. The smallest value of 0.23 occurs in the case with weakest stratification  $Ri = 0.04$ . Relative to the results of Mashayek *et al.* (2013) (denoted in figure 9 as MCP13) for the two-layer case, the peak value of  $E^C$  in the present study is smaller. A key result of Mashayek *et al.* (2013) is that there exists a narrow range of  $Ri$  for which the mixing efficiency is optimal. They report optimal mixing to occur at  $Ri = 0.16$ . Unlike their study, we do not find a narrow range of optimal efficiency. The mixing efficiency is similar for a wide range of  $Ri$  between 0.08 to 0.2. Furthermore, the

Turbulent shear layers in a uniformly stratified background

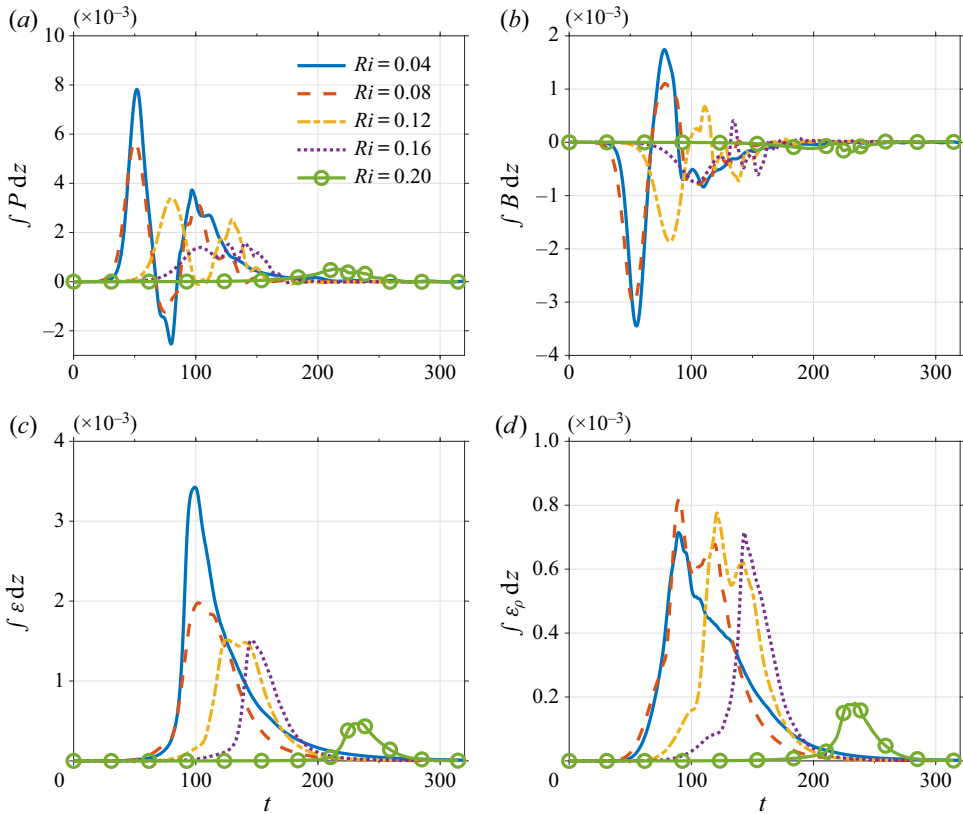


Figure 8. Evolution of the depth-integrated TKE budget and the potential energy dissipation: (a) production ( $P$ ), (b) buoyancy flux ( $B$ ), (c) TKE dissipation ( $\varepsilon$ ) and (d) dissipation of the potential energy, ( $\varepsilon_\rho$ ). Integration is performed over the region bounded by  $z = \pm 10$ .

$Ri$	$P$	$B$	$\varepsilon$	$\varepsilon_\rho$	$P/\varepsilon$	$-B/\varepsilon$	$\Gamma^C$	$E^C$
0.04	0.2298	-0.0611	0.1505	0.0444	1.5	0.41	0.3	0.23
0.08	0.1757	-0.061	0.1025	0.0458	1.7	0.6	0.45	0.31
0.12	0.1383	-0.0496	0.0781	0.0382	1.8	0.64	0.49	0.33
0.16	0.0968	-0.0321	0.0541	0.0254	1.8	0.6	0.47	0.32
0.20	0.0278	-0.0082	0.0168	0.0066	1.7	0.5	0.39	0.28

Table 2. Integrated TKE budget terms and TPE dissipation rate. The integration is taken over the region bounded by  $z = \pm 10$  and over the simulation time period. All terms are normalized by  $\Delta U^2 \delta_{\omega,0}$ .

values of  $E^C$  are significantly larger in the two-layer problem, by almost 50 % at  $Ri = 0.16$ . There are a few reasons for the smaller mixing efficiency in the present study. First, the K–H billows in the present study with stratification external to the sheared zone do not grow as large as with the two-layer density profile. Second, the use of the larger spanwise domain here allows secondary spanwise instabilities to break down the K–H billows so that the billows cannot grow as large. It is noted that the larger spanwise domain allows the seeding of broadband velocity fluctuations at the initial time to include longer-wavelength spanwise perturbations which also influence the breakdown (e.g. see

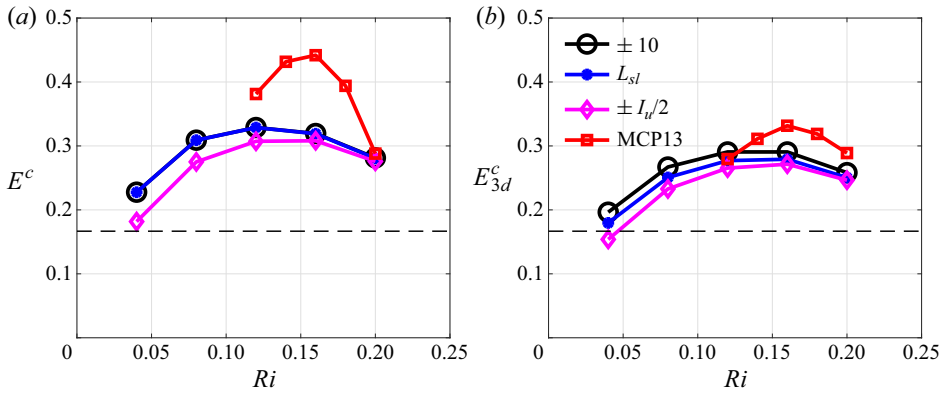


Figure 9. Effect of stratification on mixing efficiency after depth integration: (a)  $E^C$  computed by integrating  $\varepsilon_\rho$  and  $\varepsilon$  over the time duration of the simulations and (b)  $E_{3d}^C$  computed by starting integration from the time of fully developed turbulence indicated by the peak integrated dissipation rate. The depth integration is performed over the region bounded by the computational domain excluding the sponge layers  $z = \pm 10$  (black), thickness of the shear layer  $L_{sl}$  (blue) and momentum thickness  $\pm I_u/2$  (magenta). Mixing efficiency in the two-layer simulations (red) of Mashayek *et al.* (2013) (denoted MCP13) is shown for comparison. Dashed lines indicate the upper-bound value for the mixing efficiency suggested by Osborn (1980).

the spanwise snapshots in figure 3a). The study of Kaminski & Smyth (2019) indicates that strong turbulence in the shear layer at initial time can reduce the growth of K–H billows. Smaller K–H billows result in less available potential energy which is important for the subsequent turbulent mixing.

The mixing efficiency in the stage of three-dimensional turbulence ( $E_{3d}^C$ ) is found by starting the integration from the time of peak integrated dissipation rate in figure 8(c). The maximum value of  $E_{3d}^C$  of 0.29 occurs in the  $Ri = 0.12$  and 0.16 cases and is slightly smaller than the value seen in the two-layer problem. In the simulations with  $Ri \geq 0.08$ , when integrated across the shear layer and over time, the net dissipation rate decreases faster as  $Ri$  increases than the net scalar dissipation rate. The low mixing efficiency seen in the  $Ri = 0.04$  case is due to the uniquely high TKE dissipation rate. It is noted that the cumulative mixing efficiency ( $E^C$ ) and that due to fully developed turbulence ( $E_{3d}^C$ ) are not dramatically different as reported in Mashayek *et al.* (2013). In other words, the mixing efficiency induced by the rich dynamics of the secondary shear instabilities during the transition to turbulence is only as significant as the subsequent fully developed turbulence. Nonetheless, both measures of the mixing efficiency are significantly larger than the upper-bound value of  $1/6$  proposed by Osborn (1980). While the mixing efficiency  $E^C$  is similar between the  $Ri = 0.08$  and 0.2 cases, the integrated dissipation and scalar dissipation rates listed in table 2 are approximately seven times smaller in the case with stronger stratification. A large value of  $E^C$  does not imply large net mixing by K–H billows or turbulence.

#### 4. The transition layer

As illustrated in the previous section, shear instabilities and the resulting turbulence transport a significant amount of momentum and energy toward the edges of the shear layer. These turbulent fluxes induce the formation of a TL in which the local stratification  $N^2(z)$  and shear  $S(z)$  peak. Figure 9 suggests turbulent mixing in the TL can influence the overall mixing efficiency across the entire shear layer. When the dissipation and

scalar dissipation rates are integrated over the shear-layer momentum thickness, i.e.  $\pm I_u/2$ , both  $E^C$  and  $E_{3d}^C$  have smaller values than when they are integrated over the shear-layer thickness defined by the TL ( $L_{sl}$ ). Including the TL physics into the computation of mixing efficiency can increase  $E_{3d}^C$  by 17 % in the  $Ri = 0.04$  case. Furthermore, internal waves are generated inside the TL and it is unclear how the wave excitation affects the mixing efficiency (Watanabe *et al.* 2018). Therefore, it is important to understand how turbulence and wave physics in the TL influence the mixing efficiency and its parameterization.

While the mixing efficiency is significant ( $E^C = 0.28$ ) in the  $Ri = 0.2$  case, the net dissipation and scalar dissipation rate are considerably smaller than in the other cases as listed in table 2. Because of the lack of vigorous mixing in the  $Ri = 0.2$  case and, for brevity, we exclude this case from the following discussion of the TL.

#### 4.1. Development of the TL

Each of the two edges of the shear layer has a TL. For the purposes of this work, the boundaries of a TL are defined using the normalized squared buoyancy frequency,  $N^2/N_0^2$ , whose evolution is shown in figure 10. The inner and outer boundaries of the TL are demarcated by  $N^2/N_0^2 = 1$  such that the interior of the TL has  $N^2/N_0^2 > 1$ . Since the layer of enhanced  $N^2$  first develops near the centre of the shear layer during the early stage of growing K–H instability, we use  $I_u/2$  to mark the inner boundary of the TL. Note that the location of maximum  $N^2/N_0^2$  (magenta dashed line in figure 10) varies; it is closer to the inner boundary of the TL at early time and located more centrally between the two boundaries at late time. There is a sharp increase of  $N^2/N_0^2$  in the lower half of the TL before and during the growth stagnation/contraction regime for the  $Ri \leq 0.12$  cases. In all cases, as the flow transitions from being dominated by two-dimensional instabilities to fully three-dimensional turbulence, there is a time period when the peak  $N^2/N_0^2$  becomes smaller than before (approximately  $80 < t < 110$  in the  $Ri = 0.04$  and  $0.08$  cases,  $110 < t < 150$  in the  $Ri = 0.12$  case and  $140 < t < 170$  in the  $Ri = 0.16$  case). After turbulence decays at late time,  $N^2/N_0^2$  increases and concentrates at the centre of the TL. The overall value of  $N^2/N_0^2$  decreases with strengthening background stratification ( $N_0^2$ ) among cases due to the decreased turbulent mixing of momentum in the central shear layer when  $N_0^2$  is increased. At late time, the flow has arranged itself into layers with varying  $N^2/N_0^2$ . Take the  $Ri = 0.16$  case of figure 10 in which this is most evident. As seen in the vertical profile panel to the right of figure 10(d), at late time ( $t \approx 250$ ), there is a region at the centre of the shear layer where  $N^2/N_0^2 \approx 1$  above which is a layer with  $N^2/N_0^2 < 1$ . Moving outwards from this layer, there is a region of moderate  $N^2/N_0^2$  before reaching the maximum value in the centre of the TL of  $N^2/N_0^2 \approx 1.6$ . At the outer edge of the TL,  $N^2/N_0^2$  is reduced and values of  $O(1)$  are seen outside of the TL. In general, as background stratification increases, the TL becomes thinner as listed in table 1. The thickness is approximately half of the difference between the momentum thickness  $I_u$  and the shear-layer thickness  $L_{sl}$  shown previously in figure 5.

The evolution of the normalized squared rate of shear ( $S^2/S_0^2$ , where  $S = \partial\langle u \rangle/\partial z$ ) for all simulated cases is given in figure 11 where the lines bounding the TL are also shown. The TL develops as shear is reduced inside the shear layer by the influence of K–H instabilities extracting kinetic energy from the mean flow at early time. However, at the peripheries of the shear layer, shear becomes elevated as turbulence induces momentum transport away from the centre of the shear layer outwards. As such, the strongest  $S^2/S_0^2$  at late

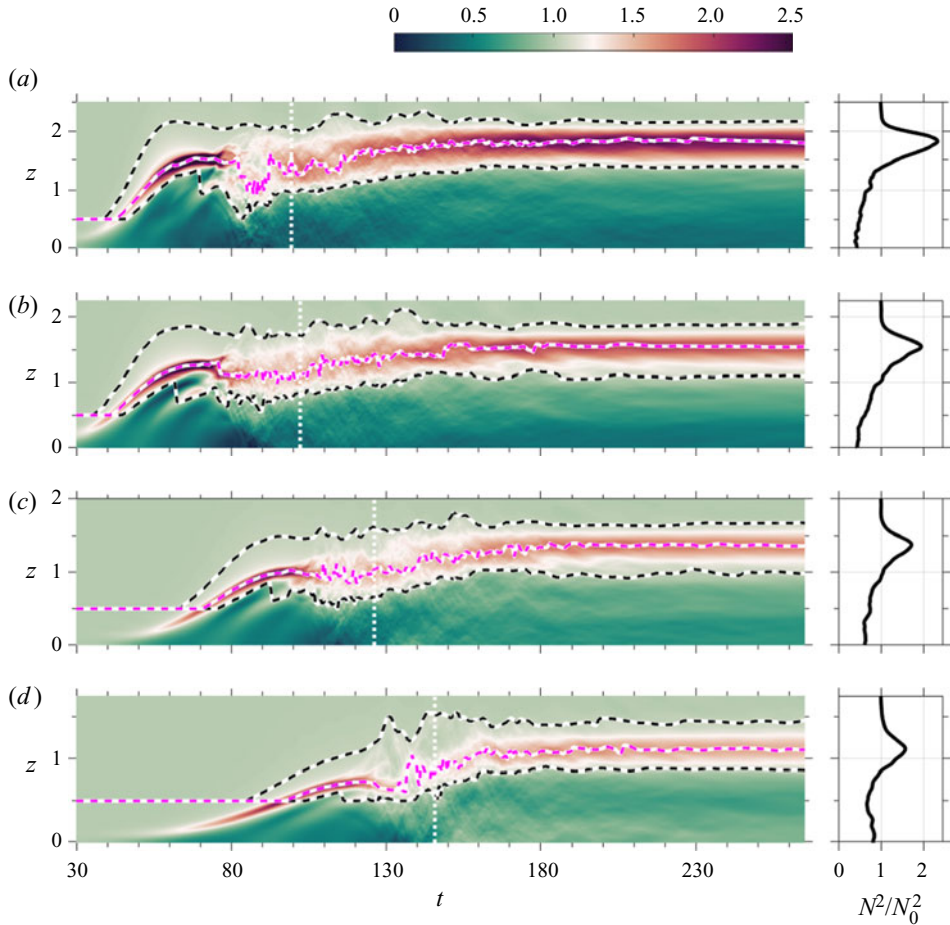


Figure 10. Evolution of the normalized squared buoyancy frequency ( $N^2/N_0^2$ ) shown using  $t - z$  contours for the (a)  $Ri = 0.04$ , (b)  $Ri = 0.08$ , (c)  $Ri = 0.12$  and (d)  $Ri = 0.16$  cases. The inner ( $TL_i$ ) and outer ( $TL_o$ ) TL boundaries are each identified using a black dashed line while the location of maximum  $N^2/N_0^2$  inside the shear layer ( $TL_m$ ) is shown with a magenta dashed line. Panels are given on the right for each case to illustrate vertical profiles of  $N^2/N_0^2$  at  $t \approx 250$  when the turbulence has subsided. The dotted white lines in all panels indicate the time of maximum dissipation rate ( $t_{3d}$ ).

time is located in the TL, close to its inner boundary, with TL shear intensity among cases increasing with strengthening  $N_0$ . At early time in all cases, a region of strong shear directly corresponds to the region of large  $N^2/N_0^2$  in the TL. The previously discussed reduction in  $N^2/N_0^2$  coincides with a brief reduction in shear in the  $Ri = 0.04$  and  $Ri = 0.08$  cases. In the more strongly stratified cases there is less significant reduction in shear. At late time in the highly stratified cases,  $S^2$  has a layered structure similar to  $N^2$ . The panel to the right of figure 11(d) shows the centre of the shear layer to have a region of moderate shear bounded by a layer of weaker shear. Farther from the centre,  $S^2/S_0^2$  increases to a peak value of approximately 0.23 before becoming negligible outside the TL.

Figure 12 shows the gradient Richardson number ( $Ri_g = N^2/S^2$ ) which is a measure of the balance between buoyancy and shear. In all cases, the inner portion of the TL has lower  $Ri_g$  than the outer half indicating that the inner portion is more influenced by effects of shear. As the flow evolves, turbulence mixes the density and momentum fields and  $Ri_g$

*Turbulent shear layers in a uniformly stratified background*

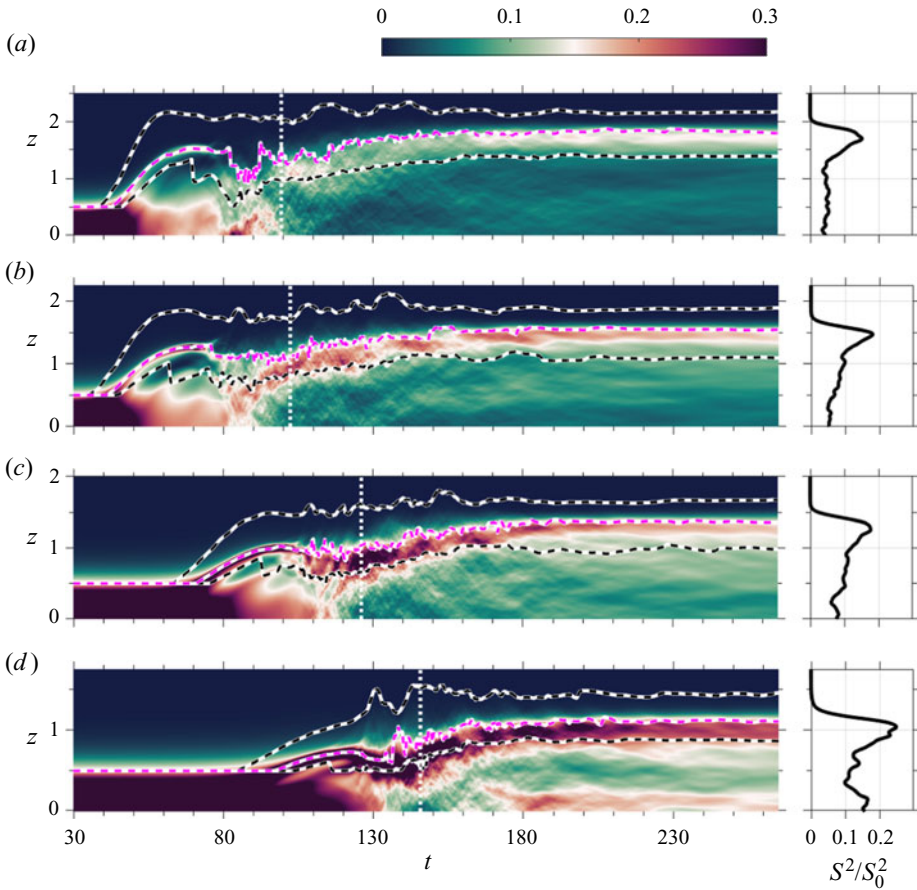


Figure 11. Similar to figure 10 but the contours show the normalized squared rate of shear ( $S^2/S_0^2$ ).

increases exceeding the critical value of 0.25 from linear stability theory (Hazel 1972). In all cases, this behaviour is observed within the TL with  $Ri_g$  beginning small and eventually becoming much larger than  $Ri_c$ . At late time, the interior of the shear layer is dominated by  $Ri_g > 0.5$  in all cases except for the  $Ri = 0.04$  case in which  $Ri_g$  takes values between  $Ri_c = 0.25$  and 0.5. In the  $Ri = 0.12$  case intermittent layers of  $Ri_g > 0.75$  and  $Ri_g > 1$  are observed, in contrast to the two-layer simulations of Mashayek & Peltier (2013) who noted that  $Ri_g \approx 0.5$  across the entire shear layer at late time in their comparable simulation. The higher  $Ri_g$  found here is further evidence of the difference in the distribution of  $S^2$  and  $N^2$  between the present case of uniformly stratified background and the case with two constant-density layers.

The development of small-scale fluctuations as the flow becomes fully turbulent leads to a rapid increase in the dissipation rate ( $\varepsilon$  in figure 13). The time of peak  $\varepsilon$ , seen when the K–H billows breakdown to three-dimensional turbulence, is delayed with increasing background stratification ( $N_0^2$ ) as follows:  $t \approx 100$  in the  $Ri = 0.04$  and  $Ri = 0.08$  cases,  $t \approx 126$  in the  $Ri = 0.12$  case and  $t \approx 145$  in the  $Ri = 0.16$  case. Furthermore, as  $N_0^2$  increases among cases,  $\varepsilon$  tends to be elevated in the TL at late time. Dissipation is strongest at the periphery near the inner boundary of the TL due to the evolving late-time instabilities.

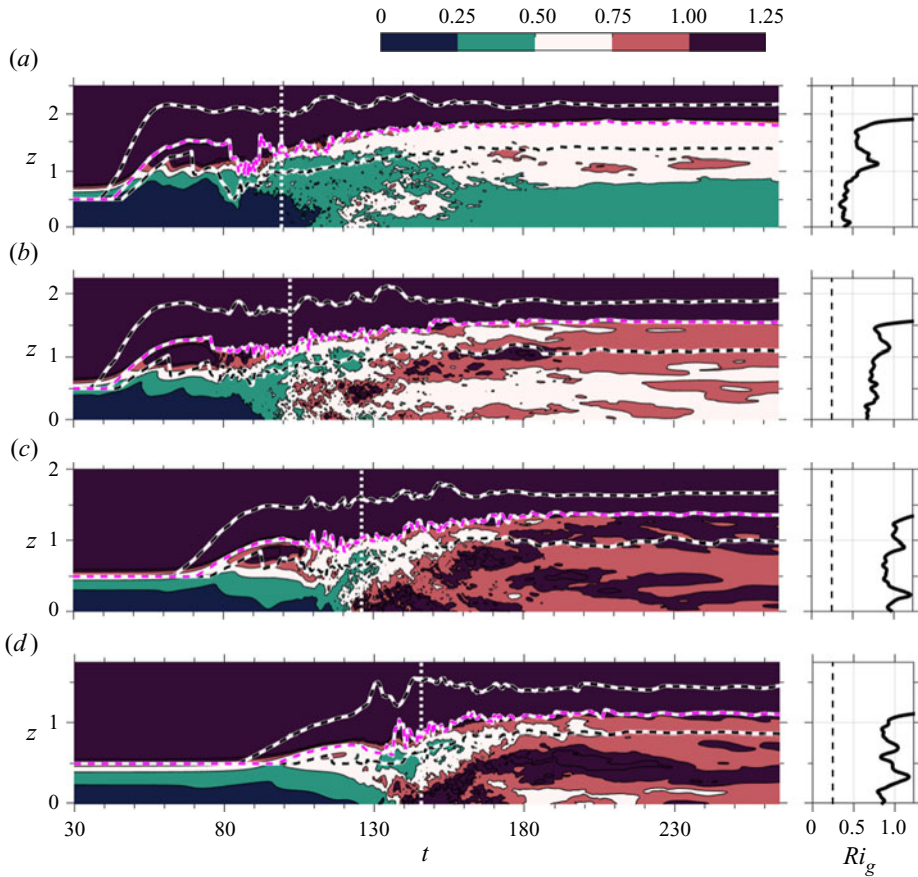


Figure 12. Similar to figure 10 but the contours show the gradient Richardson number ( $Ri_g$ ).

#### 4.2. Internal wave flux across TLs

Simulations by Watanabe *et al.* (2018) at  $Re = 6000$  and  $Ri$  up to 0.08 suggest the internal wave flux,  $\langle p'w' \rangle$ , at the TNTI to be strong. They report that the wave energy flux at the TNTI can be comparable to the dissipation in the shear layer. It is of interest to compare the role of  $\langle p'w' \rangle$  at the shear-layer edge as the Reynolds number increases from 6000 to 24 000. Figure 14(a) illustrates the evolution of  $\langle p'w' \rangle$  in the  $Ri = 0.08$  case in which its magnitude is largest during the transition from two-dimensional K–H billows to three-dimensional turbulence. As the billows grow, they create perturbations in the pressure and velocity fields that extend beyond the boundaries of the shear layer (denoted by the dashed lines in figure 14a). The perturbations generate evanescent waves whose amplitude decays exponentially with the distance away from the shear layer. The wave flux is initially positive in the upper shear layer and negative in the lower shear layer, and as a result, TKE is transported away from inside the shear layer to the outside during the growth of the K–H billows. It is noted that, since the waves are evanescent, energy does not propagate into the far field. As the shear layer grows in size, the energy that was previously transported outside contributes to the turbulent mixing in the TL. The internal wave flux in the TL is significantly weaker when the shear layer is turbulent.

### Turbulent shear layers in a uniformly stratified background

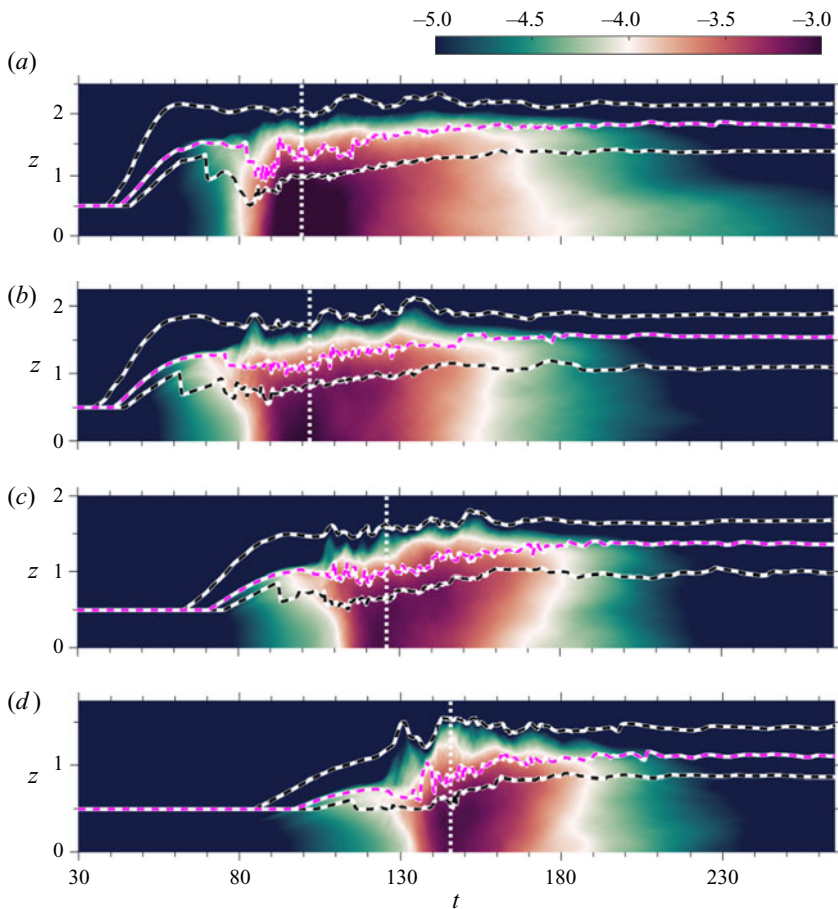


Figure 13. Similar to figure 10 but the contours show the dissipation rate ( $\log_{10}(\varepsilon)$ ).

The role of the wave flux is further examined by integrating the TKE budget from the outer edge of the lower TL to that of the upper TL. The result is shown in figure 14(b) where  $\langle p'w' \rangle_I = -\langle p'w' \rangle_{up} + \langle p'w' \rangle_{low}$  denotes the net wave energy that crosses the upper (*up*) and lower (*low*) TL interfaces. During the growth of the billows, waves transport energy outside the shear layer. As the shear layer becomes turbulent, the wave flux changes sign which deposits energy from the outside into the shear layer. During the period of turbulence, the peak inflow of the wave energy is approximately 33 % of the peak integrated dissipation rate, 22 % of the peak integrated production and 70 % of the peak integrated buoyancy flux. The wave flux seen in the present higher-*Re* study is smaller than the value reported by Watanabe *et al.* (2018).

### 5. Mixing efficiency and its parameterization

Since mixing efficiency ( $E$ ) and flux coefficient ( $\Gamma$ ) have important applications in ocean measurements and modelling, there has been a sustained effort in parametrizing such problems. It has been shown that the variability of  $E$  can be described well by the buoyancy Reynolds number ( $Re_b = \varepsilon/\nu N^2$ ) or the turbulent Froude number ( $Fr = \varepsilon/NK$ ) for homogenous stratified turbulence driven by uniform shear in an unbounded domain with

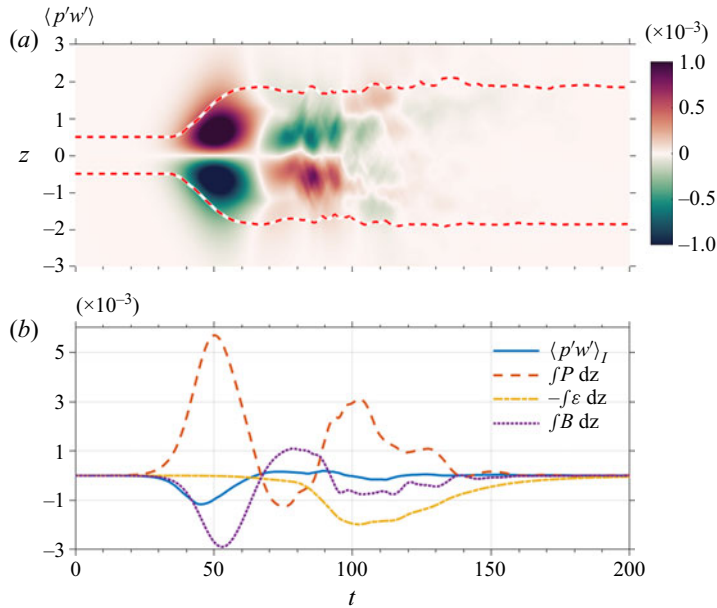


Figure 14. Internal wave flux and its influence on the TKE budget for the  $Ri = 0.08$  case: (a) temporal evolution of  $\langle p'w' \rangle$ , and (b) a comparison of the net internal wave flux across the upper and lower TLs (the dashed boundaries shown in (a)) given by  $\langle p'w' \rangle_I$  with respect to the other terms in the integrated TKE budget. Dashed lines in (a) denote the outer edges of the TLs.

uniform  $N$  (Shih *et al.* 2005; Ivey, Winters & Koseff 2008; Garanaik & Venayagamoorthy 2019). The mixing efficiency  $E$  is found to also depend on  $Pr$  and  $Ri$  (Salehipour & Peltier 2015; Salehipour *et al.* 2015). Salehipour *et al.* (2016) proposed a mixing parameterization that is based on  $Re_b$  and  $Ri$  while Mashayek *et al.* (2017b) suggested a parameterization that only relies on  $Re_b$ . In the following discussion we examine the spatial variability of  $E$  in the present configuration of a localized shear layer in a uniformly stratified fluid and discuss the results in light of the parameterization schemes proposed in the aforementioned studies. Since  $Pr = 1$  here, only the dependence on  $Re_b$ ,  $Fr$  and  $Ri$  are to be explored.

We find that the strong TL associated with the present configuration plays an important role through its mixing during the later-time period of decaying TKE. The significant turbulent activity in the TL is illustrated in figure 15 for the four cases with  $Ri \leq 0.16$ . Small-scale shear instabilities can be clearly seen in the vorticity field at times when the integrated turbulent dissipation across the shear layer is larger than the integrated production. These later-time shear instabilities grow and persist in the TL at the upper and lower edges of the shear layer and they contribute significantly to the bulk mixing in the shear layer. Therefore, it is critical for parameterization schemes to capture their effect.

Figure 16 shows the evolution of the mixing efficiency ( $E$ ) given by (2.6a,b) with the boundaries of the TL also depicted. Overall,  $E$  is much higher throughout the shear layer as K–H billows are forming. As they break down into turbulence, strong  $E$  is seen at the outer boundary of the TL while the core of the shear layer becomes relatively quiet with low  $E$ . This large  $E$  occurs after the secondary peak in production in the low  $Ri$  cases and is associated with the concentration of TKE in lobed structures. The inner boundary of the TL has relatively low  $E$ . As stratification increases and buoyancy effects suppress vertical motions,  $E$  becomes smaller at early time as can be seen by comparing the  $Ri = 0.16$  and

*Turbulent shear layers in a uniformly stratified background*

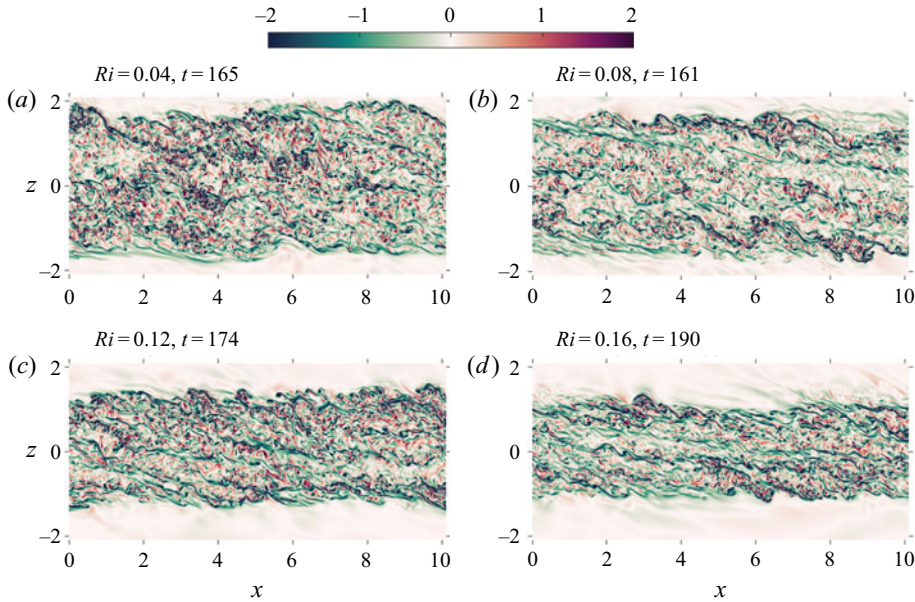


Figure 15. Cross-sectional snapshots of the spanwise vorticity ( $\omega_2$ ) fields for the (a)  $Ri = 0.04$ , (b)  $Ri = 0.08$ , (c)  $Ri = 0.12$  and (d)  $Ri = 0.16$  cases.

$Ri = 0.04$  cases in figure 16. At late time, the majority of high-efficiency mixing occurs within or above the TL.

To parametrize mixing efficiency, it is necessary to relate a bulk mixing efficiency to the bulk values of Reynolds number, Froude number and Richardson number. The time-dependent bulk values are obtained by integration across the shear layer from the outer edge of the bottom TL to that of the top TL. This choice of integration domain (thickness denoted by  $L_{sl}$ ) encompasses the spatial region of significant turbulent dissipation. We also focus the analysis on the temporal period with significant mixing, namely the regime of fully developed turbulence which commences after the time of the peak integrated  $\varepsilon$ , similar to Salehipour *et al.* (2016) and Mashayek *et al.* (2017b). In the discussion to follow, the bulk mixing efficiency ( $E_{3d}$ ), bulk buoyancy Reynolds number ( $Re_b$ ), bulk turbulent Froude number ( $Fr$ ) and bulk Richardson number ( $Ri_b$ ) are computed as follows:

$$\left. \begin{aligned} E_{3d}(t) &= \frac{\int_{L_{sl}} \varepsilon_\rho \, dz}{\int_{L_{sl}} \varepsilon_\rho + \varepsilon \, dz}, & Re_b(t) &= \frac{\int_{L_{sl}} \varepsilon \, dz}{\int_{L_{sl}} \nu N^2 \, dz}, \\ Fr(t) &= \frac{\int_{L_{sl}} \varepsilon \, dz}{\int_{L_{sl}} NK \, dz}, & Ri_b &= \frac{\Delta\rho_{sl} g L_{sl}}{\rho_0 \Delta U_{sl}^2}. \end{aligned} \right\} \quad (5.1)$$

Here  $\Delta\rho_{sl}$  and  $\Delta U_{sl}$  denote the density and velocity change across the spatial integration domain.

The dependence of mixing efficiency ( $E_{3d}$ ) on  $Re_b$  is shown in figure 17(a). Shih *et al.* (2005) suggested three regimes of turbulent mixing: an energetic regime ( $Re_b > 10^2$ ),

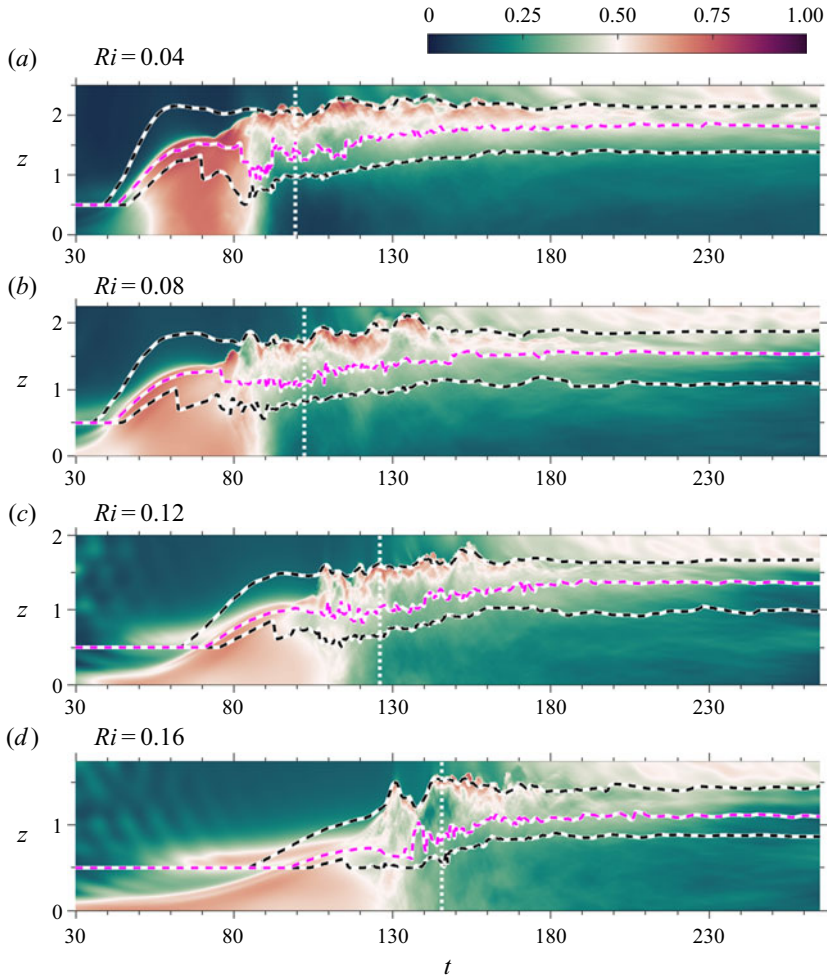


Figure 16. Similar to figure 10 but the contour shows the mixing efficiency ( $E$ ).

an intermediate regime ( $7 \leq Re_b \leq 10^2$ ) and a diffusive regime ( $Re_b < 7$ ). These three regimes are also exhibited in the present study although the values of  $Re_b$  used to separate the regimes are slightly different. In the present study,  $E_{3d}$  decreases with increasing  $Re_b$  in the energetic regime ( $Re_b$  is as large as 540 in the  $Ri = 0.04$  case). During the intermediate regime ( $40 < Re_b < 100$ ),  $E_{3d}$  remains relatively constant at the value of 0.3 in the cases with  $0.08 \leq Ri \leq 0.16$ . The mixing efficiency decreases monotonically in the diffusive regime ( $Re_b < 40$ ).

The flux coefficient ( $\Gamma_{3d}$ ) is also often used to quantify mixing. From mixing efficiency, the flux coefficient can be computed as  $\Gamma_{3d} = E_{3d}/(1 - E_{3d})$ . Figure 17(b) shows the flux coefficient also varies with  $Re_b$  in three distinctive regimes similar to the mixing efficiency. The peak value of  $\Gamma_{3d}$  is approximately 0.43 which is more than twice larger than the upper-bound value of 0.2 suggested by Osborn (1980). Furthermore,  $\Gamma_{3d}$  remains larger than 0.2 over the entire lifespan of turbulence in the cases with  $Ri \geq 0.08$ . The flux coefficient  $\Gamma_{3d}$  peaks at a smaller value of 0.32 in the  $Ri = 0.04$  case and decreases to below 0.2 in the diffusive regime.

Turbulent shear layers in a uniformly stratified background

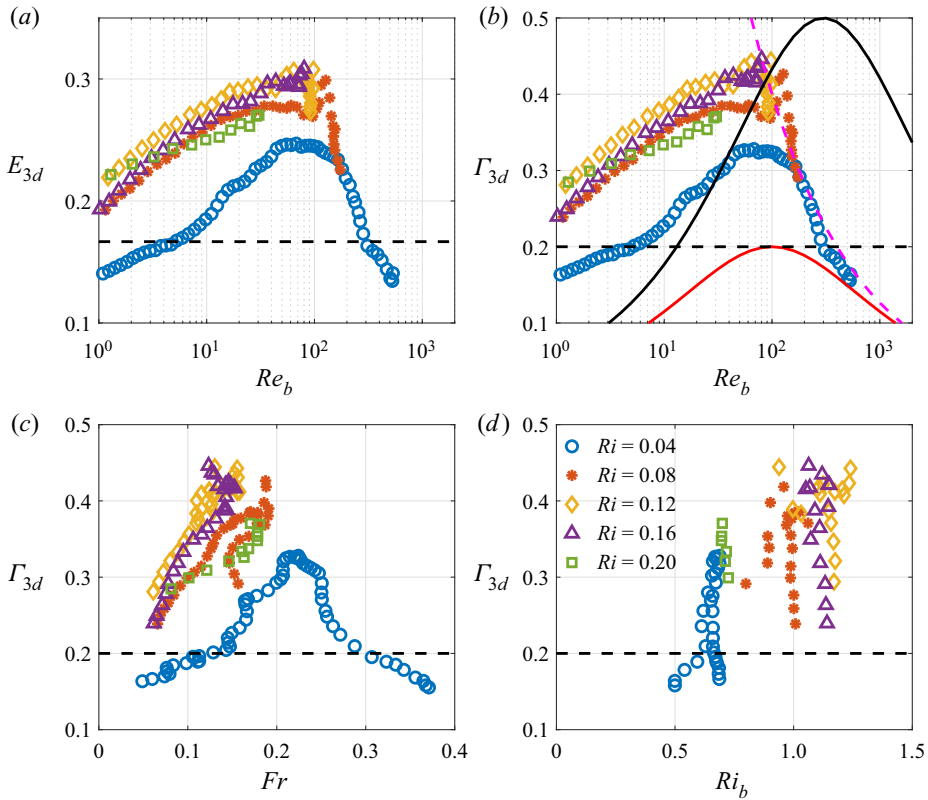


Figure 17. Effect of buoyancy Reynolds number ( $Re_b$ ) on (a) mixing efficiency ( $E_{3d}$ ), and (b) flux coefficient ( $\Gamma_{3d}$ ) and the effect of (c) turbulent Froude number ( $Fr$ ) and (d) bulk Richardson number ( $Ri_b$ ) on the flux coefficient during the turbulent phase. The dashed black lines indicate the values of  $E_{3d} = 1/6$  and  $\Gamma_{3d} = 0.2$  suggested by Osborn (1980). The dashed magenta line in panel (b) indicates the parameterization,  $\Gamma_{3d} = 4Re_b^{-1/2}$  for  $Re_b > 10^2$  in the  $Ri = 0.04$  case. The solid black and red lines in panel (b) denote the upper and lower bounds, respectively, of the parameterization proposed by Mashayek *et al.* (2017b).

Shih *et al.* (2005) indicated that the flux coefficient decreases as  $\Gamma_{3d} = 2Re_b^{-1/2}$  in the energetic regime. We also find that  $\Gamma_{3d} \propto Re_b^{-1/2}$  in the  $Ri = 0.04$  case although its value is substantially larger here leading to a proportionality coefficient of 4 as shown in figure 17(b). During the intermediate regime, the flux coefficient remains relatively constant with a value ranging from 0.33 in the  $Ri = 0.04$  case to approximately 0.43 in the other three cases. These values are larger than that of 0.2 reported in Shih *et al.* (2005). While Shih *et al.* (2005) asserted that turbulent mixing in the diffusive regime is driven mainly by molecular diffusivity and independent of  $Re_b$ , the turbulent mixing in the present study is significantly higher than the molecular counterpart and, indeed, varies with  $Re_b$  when  $7 \leq Re_b \leq 40$ . Nonetheless, the mixing convention of Shih *et al.* (2005) is kept in the present study for ease of comparison.

The upper and lower bounds for  $\Gamma_{3d}$  suggested by Mashayek *et al.* (2017b) are also included in figure 17(b) for comparison. Inherently, the dependency of the flux coefficient on  $Re_b$  in the present study agrees better with the suggested parameterization using homogenous stratified turbulence in Shih *et al.* (2005) than the one in Mashayek *et al.* (2017b). In the latter scheme,  $\Gamma_{3d}$  peaks at a transitional  $Re_b$  with values ranging

from 100 to 300. As  $Re_b$  increases in the shear-dominated regime or decreases in the buoyancy-dominated regime,  $\Gamma_{3d}$  decreases similarly at the same rate. The  $Ri \leq 0.16$  cases in the present study indicate  $\Gamma_{3d}$  peaks at  $Re_b \approx 10^2$  and, furthermore, it does not decrease similarly as  $Re_b$  deviates from the transitional value. The  $Ri \leq 0.16$  cases shows the presence of an intermediate regime ( $40 \leq Re_b \leq 10^2$ ) in which  $\Gamma_{3d}$  remains relatively constant at values closer to the upper bound than the lower bound given by Mashayek *et al.* (2017b). We note that the parameterization suggested in Mashayek *et al.* (2017b) is based on both DNS of a shear layer with a two-layer density profile and observational data collected at sites where stratification and shear profiles are space-filling unlike their DNS set-up. It is unclear how the disparity between the DNS and the observational data influences the suggested parameterization. Nonetheless, the  $Re_b$  dependence of  $\Gamma_{3d}$  seen in the present study suggests further evaluation of the parameterization.

Beside  $Re_b$ , the turbulent Froude number ( $Fr(t)$ ) can be a well-suited parameter for mixing parameterization of homogenous stratified turbulence (Ivey & Imberger 1991; Shih *et al.* 2000; Howland, Taylor & Caulfield 2020). The metric shows the competition between turbulent time scale ( $K/\varepsilon$ ) and buoyancy time scale ( $N^{-1}$ ) so it can be used to describe the local state of stratified shear turbulence. For weakly stratified turbulence ( $Fr > 1$ ), the flux coefficient decreases as  $Fr^{-2}$  while it remains relatively constant for strongly stratified turbulence ( $Fr < 1$ ) (Garanaik & Venayagamoorthy 2019). In the present study we also observe two regimes of  $Fr$  as shown in figure 17(c). In the  $Ri = 0.04$  case the two regimes are delineated by  $Fr \approx 0.2$ , a value somewhat smaller than unity. As  $Fr$  increases or decreases from this value,  $\Gamma_{3d}$  decreases which suggests the optimal rate of mixing occurs at  $Fr \approx 0.2$  in this case. The other four cases with  $Ri \geq 0.08$  show  $\Gamma_{3d}$  also peaks at  $Fr$  less than 0.2 and it decreases as  $Fr$  decreases. Our results agree well with Maffioli *et al.* (2016) who, in homogenous stationary stratified turbulence DNS, found optimal mixing at  $\varepsilon/Nu^2 = 0.3$ , which converts to  $Fr = \varepsilon/NK = 0.2$  upon taking  $u^2 = 2K/3$ .

The bulk Richardson number ( $Ri_b(t)$ ) is also used as a descriptor of the state of stratified shear turbulence and a quantity to potentially correlate the flux coefficient. Figure 17(d) shows the dependency of the flux coefficient on  $Ri_b$ . In all simulated cases,  $\Gamma_{3d}$  decreases at constant  $Ri_b$  during the later-time intermediate and diffusive regimes. The late-time constant value of  $Ri_b$  is as large as 1.2 in the  $Ri = 1.2$  case while it is approximately 0.7 in the  $Ri = 0.04$  case. The dependence on  $Ri_b$  shows a qualitative change among the different  $Ri$  cases and it is not possible to infer a common correlative trend. It is critical to emphasize that efficient turbulent mixing persists even at values of  $Ri_b$  as large as 1.2, approximately two times larger than with the two-layer density profile. This is a direct consequence of strong turbulent activity in the sheared TLs at the edge of the shear layer which expands the vertical extent of the stratified region with active mixing. Salehipour *et al.* (2016) proposed a mixing parameterization in which the maximum mixing efficiency occurs at  $Ri_b = 0.4$  and turbulent mixing cuts off at  $Ri_b = 1$ . The cases with  $Ri \geq 0.08$  in the present study shows that the mixing efficiency and flux coefficient peak as  $Ri_b$  reaches values as large as 1.2. Clearly, the formation of TLs modifies the range of  $Ri_b$  for which turbulent mixing is important. Therefore, it is important for any  $Ri_b$ -based mixing parameterizations to include TL dynamics.

A choice for the turbulent diffusivity ( $K_\rho$ ) provides a turbulence closure for the buoyancy flux since, by definition,  $K_\rho = B/N^2$ . Retaining only the irreversible part of the buoyancy flux leads to  $K_\rho = \varepsilon_\rho/N^2 = \Gamma_{3d} \varepsilon/N^2$ . For  $Pr = 1$ , it follows that  $K_\rho = \Gamma_{3d} \kappa Re_b$ . Osborn (1980) chose  $\Gamma_{3d} = 0.2$  leading to a linear dependence of  $K_\rho = 0.2\kappa Re_b$  on the buoyancy Reynolds number for all values of  $Re_b$ . To assess the Osborn parameterization, a bulk value of turbulent diffusivity is computed from the simulation

Turbulent shear layers in a uniformly stratified background

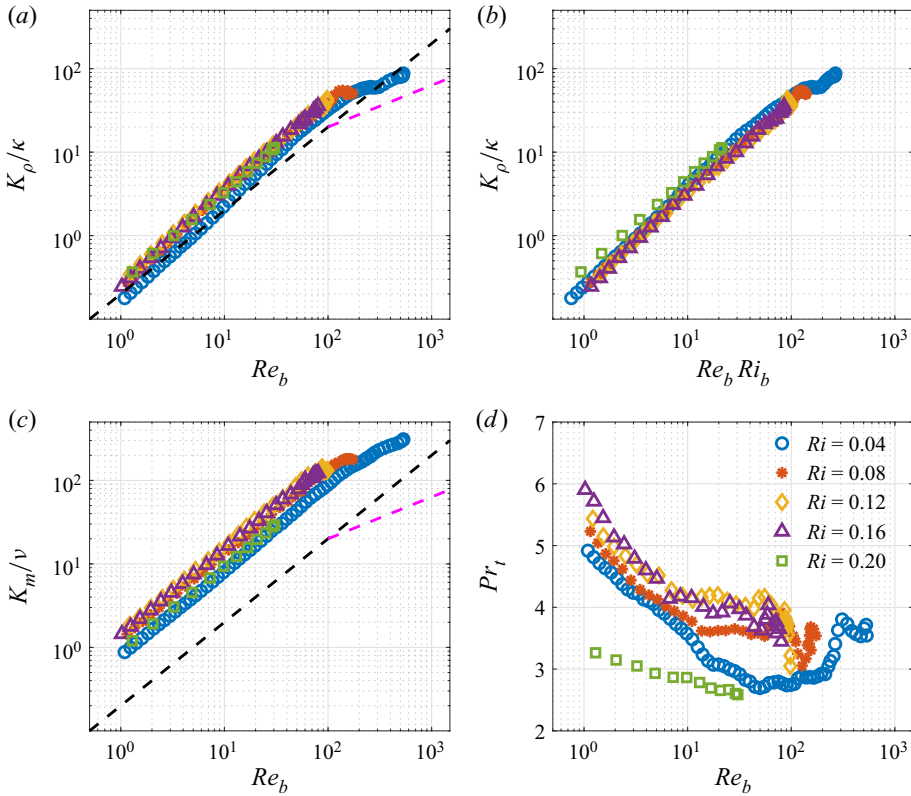


Figure 18. Effect of (a) buoyancy Reynolds number ( $Re_b$ ) and (b) combined buoyancy Reynolds number and bulk Richardson numbers ( $Re_b Ri_b$ ) on turbulent diffusivity ( $K_\rho$ ). Variability of turbulent viscosity ( $K_m$ ) and turbulent Prandtl number ( $Pr_t$ ) on  $Re_b$  are shown in panels (c) and (d), respectively. The dashed black lines in panels (a,c) indicate the parameterization,  $K_\rho/\kappa = K_m/\nu = 0.2Re_b$ , from Osborn (1980) with the assumption of  $Pr = Pr_t = 1$ . The dashed magenta lines in panels (a,c) indicate the parameterization,  $K_\rho/\kappa = K_m/\nu = 2Re_b^{1/2}$  for  $Re_b > 10^2$ , from Shih *et al.* (2005) with the same assumption of  $Pr_t = 1$ .

data as  $K_\rho(t) = \int \varepsilon_\rho dz / \int N^2 dz$  where the  $z$ -integration is over  $L_{sl}$ . Figure 18(a) shows the turbulent diffusivity to exhibit piecewise dependence on  $Re_b$  similar to the piecewise dependence of  $\Gamma_{3d}$  on  $Re_b$ . Disregarding the decrease of  $\Gamma_{3d}$  in the diffusive regime,  $K_\rho$  exhibits a linear dependence on  $Re_b$  for  $Re_b \leq 10^2$  similar to Osborn’s model. However, the model underestimates  $K_\rho$  which suggest a higher constant value of the flux coefficient can improve said model. In the energetic regime ( $Re_b > 10^2$ ),  $K_\rho$  is found to be proportional to  $Re_b^{1/2}$  similar to the results of Shih *et al.* (2005) although the proportionality coefficient is larger in the present study. It should be noted that Salehipour & Peltier (2015) also found the  $Re_b$ -dependence for  $K_\rho$  in shear layers with a two-layer density profile to be similar to the result in Shih *et al.* (2005), e.g. see their figure 5.

Taking into account the effects of both  $Re_b$  and  $Ri_b$ , it is found that  $K_\rho$  can be parametrized based on the product of  $Re_b$  and  $Ri_b$  as shown in figure 18(b). The choice of  $Re_b Ri_b \approx \varepsilon/\nu S^2$  is equivalent to using  $S$  as a characteristic inverse time scale rather than  $N$  in the mixing parameterization. This parameterization scheme is promising because it prescribes  $K_\rho$  over the entire range of  $Re_b$ , unlike the piecewise dependence observed when only  $Re_b$  is used. It is noted that the bulk parameters in the present study do not

extend sufficiently into the energetic regime (only the  $Ri = 0.04$  case includes a large range of  $Re_b$ ) and additional simulations at a higher Reynolds number are required to test whether this parameterization works well for the energetic regime.

We now move to the turbulent viscosity ( $K_m$ ) and its parameterization. By definition of the turbulent viscosity, it follows that  $K_m = P/S^2$ , where  $P$  is the turbulent production. The equilibrium assumption for the TKE equation is used to write  $P = \varepsilon + B$  and the part of  $B$  responsible for irreversible mixing ( $\varepsilon_\rho$ ) is retained so that the turbulent viscosity becomes  $K_m = (\varepsilon + \varepsilon_\rho)/S^2$ . A bulk value of  $K_m(t)$  is computed here using bulk (integrals over  $L_{sl}$ ) values of  $\varepsilon$ ,  $\varepsilon_\rho$  and  $S^2$ . Figure 18(c) shows that  $K_m$  cannot be described by the Osborn model in this flow. Results from Shih *et al.* (2005) for homogeneous shear flow indicate that  $Pr_t = 1$  in the intermediate regime and decreases in the energetic regime (where  $Ri_b$  is also low) to  $Pr_t \approx 0.6$ . In the present study  $Pr_t$  exceeds 2.5 in all simulated cases for all mixing regimes. These higher values of  $Pr_t$  are related to the higher  $Ri_b$  in this problem. For example,  $Ri_b$  increases from its initial value of 0.04 to 0.5 during  $30 < t < 60$  when the flow transitions to turbulence and into the energetic regime. Thus, unlike homogenous shear flow, the energetic regime with large  $Re_b$  is accompanied by a significant increase of  $Ri_b$  in this flow and, consequently,  $Pr_t \sim Ri_b/E_{3d}$  is large even in the energetic regime. Furthermore, once buoyancy becomes sufficiently strong to bring  $Re_b$  down to  $\approx 100$ ,  $Pr_t(t)$  increases with decreasing  $Re_b(t)$  because  $E_{3d}$  commences a decrease from its peak value.

## 6. Discussion and conclusions

In the present study DNS of a shear layer with uniform density stratification were performed to investigate turbulence and mixing at a Reynolds number ( $Re$ ) of 24 000, a high value for DNS. The stratification in the chosen problem is extensive or domain filling in contrast to the well-studied case of continuous stratification between two layers, each with constant density, where the stratification is spatially compact and limited to the zone with shear. The background stratification ( $N_0$ ) is varied over a wide range to examine the effects of buoyancy,  $Ri = 0.04$ – $0.2$ , where  $Ri$  is the gradient Richardson number at the shear-layer centre. The simulation results are analysed to highlight the important effects of the uniform stratification outside the shear layer on the evolution of shear-layer turbulence. Furthermore, the results on mixing are contrasted with those of homogenous stratified shear turbulence (e.g. Shih *et al.* 2005) and of shear-layer turbulence between two layers of uniform density (a canonical two-layer density profile, e.g. Salehipour *et al.* 2016; Mashayek *et al.* 2017b) as well as the mixing parameterization scheme of Osborn (1980).

Kelvin–Helmholtz shear instabilities develop in all cases. After the K–H instability develops, a myriad of secondary instabilities are seen to follow. The dynamics of secondary instabilities are as rich as those that arise in the stratified shear layer with a two-layer density profile. The secondary instabilities are driven by both enhanced shear in the eyelids and in the braids between K–H billows as well as by convection due to the unstable density gradient associated with the roll-up of the billows. Secondary convective instability is seen in the core as well as the eyelids of the K–H billows. As the secondary instabilities develop, the shear layer contracts, as indicated by the decrease of momentum thickness, for a short time in the  $Ri = 0.04$  and  $Ri = 0.08$  cases, a feature that has not been observed in similar simulations at lower  $Re$  (Pham *et al.* 2009; Pham & Sarkar 2010; Watanabe *et al.* 2018). Counter-gradient momentum transport (CGMT) and counter-gradient buoyancy flux (CGBF) occur during the contraction period leading

to negative shear production and an increase in the MKE. Strong stratification tends to inhibit the growth of CGMT and CGBF since they do not occur in the  $Ri \geq 0.12$  cases.

The shear and stratification in the sheared zone evolve to profiles which are different from those found in the canonical two-layer problem. Mashayek *et al.* (2013) and Salehipour *et al.* (2016) find that the largest value of the evolving bulk Richardson number  $Ri_b(t)$  in the problem with a two-layer density profile is 0.5. Here,  $Ri_b(t)$  can reach up to 1.2. Furthermore, multiple layers with differing  $Ri_g$  including  $Ri_g > 1$  form.

While the rich dynamics of the secondary instabilities in the present case with domain-filling stratification are similar to those for a two-layer density profile, the mixing efficiency in the present study is significantly different. Mashayek *et al.* (2013) who used a two-layer density profile found a narrow range of  $Ri$  with an optimal rate of turbulent mixing, and the cumulative mixing efficiency ( $E^C$  based on the mixing over the entire flow evolution) peaks at a value of 0.45 when  $Ri = 0.16$ . For the present case of uniform stratification, we find  $E^C$  to be considerably smaller (approximately 0.33) in the cases with  $Ri \geq 0.08$ . Also,  $E^C$  remains relatively constant among these cases suggesting a much wider range of  $Ri$  for optimal turbulent mixing.

A TL with elevated local stratification and shear forms at each edge of the shear layer owing to vertical turbulent fluxes which transport mass and momentum outward from the central region. The two TLs bound a central zone where the shear and stratification profiles are quite different from their initial shape. The central zone takes the form of a layer with some variability of shear and stratification around nominal constants whose value depends on the background stratification ( $Ri_0$ ). As  $Ri_0$  increases, the TL becomes thinner. The local  $N^2(z)$  in the TL of the present configuration can be more than twice larger than  $N_0^2$ , in contrast to the two-layer density profile where  $N^2$  in the TL does not exceed its initial peak. Despite having the largest local  $N^2$ , the TL sees significant turbulence at late time long after turbulence at the shear-layer centre has subsided and the local value of  $Ri_g$  becomes larger than the critical value of 0.25. The TL exhibits high  $Re_b = O(10^2)$  with mixing as efficient as at the shear-layer centre.

Background  $N_0^2$  supports strong internal wave flux across the TL as previously reported by Watanabe *et al.* (2018). However, the magnitude of the wave flux (33 % of the peak spatially integrated dissipation rate) is smaller at the higher  $Re$  of the present DNS. Since the route to turbulence in the shear layer is different at high  $Re$ , so is the wave flux. It is worth noting that, unlike the far-field internal waves seen in Pham *et al.* (2009), the waves in the present study with weaker  $N_0$  are evanescent and do not propagate far from the TL.

The dependence of mixing efficiency ( $E_{3d}$ ) and flux coefficient ( $\Gamma_{3d} = E_{3d}/(1 - E_{3d})$ ) on buoyancy Reynolds number ( $Re_b$ ), turbulent Froude number ( $Fr$ ) and bulk Richardson number ( $Ri_b$ ) during the turbulent phase is found to be different from that seen in the shear layer with a two-layer density profile. The dependence is closer to statistically homogeneous turbulence forced by uniform shear and uniform stratification. A possible reason is that, during the regime of vigorous turbulence, the present high- $Re$  shear layer in a uniformly stratified fluid evolves to shear and stratification profiles (e.g. the late-time profiles in figures 10 and 11) closer to the homogeneous shear problem over a large portion of the shear layer. For the same value of  $Ri$ , the uniformly stratified shear layer has a larger initial background potential energy. Using a two-layer density profile, Mashayek *et al.* (2017b) suggested that  $\Gamma_{3d}(Re_b)$  increases as  $Re_b^{1/2}$  until a maximum of approximately 0.5, and subsequently decreases as  $Re_b^{-1/2}$ . The flux coefficient in the present study exhibits three regimes of turbulent mixing similar to the finding of Shih *et al.* (2005) for homogeneous sheared turbulence: a diffusive regime at low  $Re_b$  where  $\Gamma_{3d}$

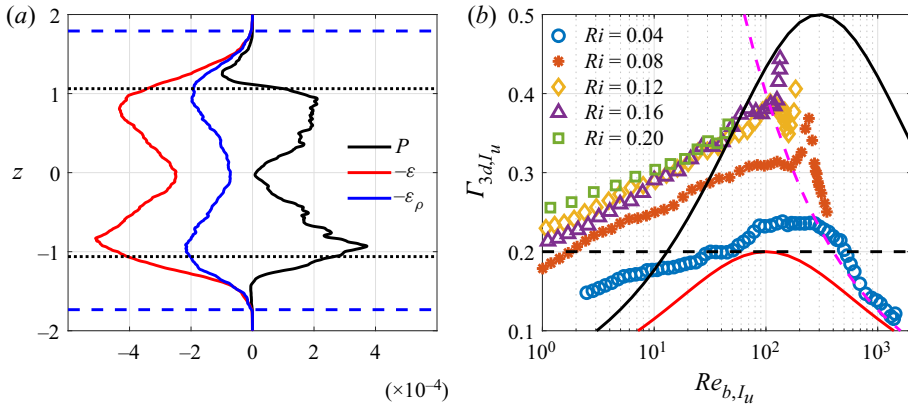


Figure 19. Effect of alternative choices,  $I_u$  and  $L_{sl}$ , for the length scale of the turbulent zone. (a) Profiles of turbulent production ( $P$ ), dissipation ( $\varepsilon$ ) and dissipation of the potential energy ( $\varepsilon_\rho$ ) at time  $t = 152$  in the  $Ri = 0.12$  case. The dotted black lines and dashed blue lines mark the boundaries of the shear layer with  $\pm I_u/2$  and  $L_{sl}$ , respectively. (b) Dependence of flux coefficient ( $\Gamma_{3d,I_u}$ ) on buoyancy Reynolds number ( $Re_{b,I_u}$ ) when the involved variables are integrated over  $\pm I_u/2$  instead of over  $L_{sl}$ . The dashed black lines in panel (b) indicate the value of  $\Gamma_{3d} = 0.2$  suggested by Osborn (1980), while the solid black and red lines denote the upper and lower bounds, respectively, of the Mashayek *et al.* (2017b) parameterization. The dashed magenta line indicates the parameterization,  $\Gamma_{3d} = 4Re_b^{-1/2}$  for  $Re_b > 10^2$  in the  $Ri = 0.04$  case also shown in figure 17(b).

monotonically increases, an intermediate regime in which  $\Gamma_{3d}$  remains relatively constant and an energetic regime where  $\Gamma_{3d} \sim Re_b^{-1/2}$ . When compared with the results of Shih *et al.* (2005), there are some quantitative differences, e.g. the cases with  $Ri \geq 0.08$  have higher values of  $\Gamma_{3d}$ . We note that, different from Shih *et al.* (2005), Portwood *et al.* (2019) reported that  $\Gamma \propto Re_b^{-1/2}$  dependence does not exist for  $100 < Re_b < 1000$  in a recent DNS study with similar set-up. They argue that a transient effect in Shih *et al.* (2005) is the possible cause of the scaling. Our results support the validity of the  $\Gamma \propto Re_b^{-1/2}$  scaling. When  $\Gamma_{3d}$  is parametrized as a function of the Froude number ( $Fr$ ), the flux coefficient in the present study also exhibits similar dependence as observed in the study of homogeneous stratified forced turbulence of Maffioli *et al.* (2016). The peak value of  $\Gamma_{3d}$  occurs at  $Fr = \varepsilon/NK \approx 0.2$  and it decreases as  $Fr$  deviates from this value.

The results for the mixing-efficiency parameterization depend on the choice employed for the vertical length scale of the shear layer. Figure 19(a) shows that the vertical profiles of turbulent production, TKE dissipation and TPE dissipation extend outside the boundaries of the shear layer marked by  $\pm I_u/2$ . Clearly, the shear-layer thickness ( $L_{sl}$ ) is able to include the entire turbulent mixing zone better than  $I_u$ . The relationship between the flux coefficient and the buoyancy Reynolds number (figure 19b) using  $\pm I_u/2$  has some differences with that obtained using  $L_{sl}$  (figure 17b). Comparison of figures 17(b) to 19(b) reveals the agreement with the scaling  $\Gamma_{3d} = 4Re_b^{-1/2}$  in the energetic regime ( $Re_b > 10^2$ ) in the  $Ri = 0.04$  case is less when  $I_u$  is used as the vertical length scale. The flux coefficient decreases monotonically with decreasing  $Re_b$  in the intermediate regime ( $40 < Re_b < 100$ ) while it remains relatively constant when  $L_{sl}$  is used as the length scale in the cases with  $0.08 \leq Ri \leq 0.16$ . The values of the flux coefficient using  $\pm I_u/2$  are considerably smaller in the intermediate regime for all cases since the high-efficiency mixing in the TLs is excluded.

The mixing efficiency in the cases with  $Ri \geq 0.08$  exceeds Osborn's model value of  $1/6$  over the entire turbulent state. Similar to the results of Salehipour *et al.* (2016),  $E_{3d}$  also exhibits a dependence on  $Ri_b$ . While Salehipour *et al.* (2016) suggested that the mixing efficiency reaches its peak value of approximately 0.33 when  $Ri_b = 0.4$  and is saturated when  $Ri_b = 1$ ,  $E_{3d}$  in the  $Ri = 0.12$  case reaches its maximum value of 0.31 when  $Ri_b$  is as large as 1.2. The larger  $Ri_b$  found in the present study is directly related to the stronger stratification in the TLs. The turbulent diffusivity ( $K_\rho$ ) and turbulent viscosity ( $K_m$ ) are larger than Osborn's model prediction as well as Shih *et al.* (2005). During entry into the initial energetic regime when  $Re_b$  increases to  $> 100$ ,  $Ri_b$  also becomes large so that the turbulent Prandtl number ( $Pr_t \sim Ri_b/E_{3d}$ ) is larger than in Shih *et al.* (2005) or Salehipour *et al.* (2016). In the other regimes,  $Pr_t$  increases with decreasing  $Re_b$  similar to other flows.

The results of the present study further confirm that turbulent mixing and its parameterization is sensitive to flow conditions including the shape of initial velocity and density profiles. The evolution of  $Ri_b$  is significantly different between two-layer and constant stratification profiles since local  $N^2(z)$  and  $S^2(z)$  evolve differently. In order for a mixing parameterization to be generally applicable, future efforts would benefit by going beyond the use of bulk parameters to account for problem-dependent variability of local shear and stratification. It should be noted the parameterization of mixing efficiency may require multiple parameters; some of which are not yet considered in the present study. The value of the molecular Prandtl number ( $Pr = 1$ ) in the present study is smaller than in oceanic flows where  $Pr$  varies from 7 to 700. The mixing efficiency  $E^C$  has been shown to decrease at higher  $Pr$  (Smyth *et al.* 2001; Salehipour *et al.* 2015) for the two-layer density profile. In light of the significant reduction in  $E^C$  between the two-layer density profile and uniform stratification (e.g. see figure 9), a further decrease due to higher- $Pr$  effect would bring  $E^C$  closer to the value of  $1/6$  used in Osborn's model.

**Acknowledgements.** The authors appreciate the LSA code which was provided by W. D. Smyth. The authors would also like to acknowledge the use of the Department of Defense HPCMP Cray XC40 system, Gordon, which was used for all simulations.

**Funding.** This work was supported by the Office of Naval Research (A.V.D. and S.S., grant numbers N00014-15-1-2718 and N00014-20-1-2253); and the National Science Foundation (H.T.P., grant number OCE-1851390).

**Declaration of interests.** The authors report no conflict of interest.

#### Author ORCIDs.

 Hieu T. Pham <https://orcid.org/0000-0002-2034-5466>;

 Sutanu Sarkar <https://orcid.org/0000-0002-9006-3173>.

#### REFERENCES

- ARRATIA, C. 2011 Non-modal instability mechanisms in stratified and homogeneous shear flow. PhD thesis, Ecole Polytechnique X.
- ARRATIA, C., CAULFIELD, C.P. & CHOMAZ, J.M. 2013 Transient perturbation growth in time-dependent mixing layers. *J. Fluid Mech.* **717**, 90–133.
- BRUCKER, K. & SARKAR, S. 2007 Evolution of an initially turbulent stratified shear layer. *Phys. Fluids* **19**, 101105.
- CAULFIELD, C.P. & PELTIER, W.R. 2000 The anatomy of the mixing transition in homogeneous and stratified free shear layers. *J. Fluid Mech.* **413**, 1–47.
- DONG, W., TEDFORD, E.W., RAHMANI, M. & LAWRENCE, G.A. 2019 Sensitivity of vortex pairing and mixing to initial perturbations in stratified shear flows. *Phys. Rev. Fluids* **4**, 063902.
- DRAZIN, P.G. 1958 The stability of a shear layer in an unbounded heterogeneous inviscid fluid. *J. Fluid Mech.* **4** (2), 214–224.

- FRITTS, D. 1982 Shear excitation of atmospheric gravity waves. *J. Atmos. Sci.* **39**, 1936–1952.
- FRITTS, D.C., BAUMGARTEN, W.K., WERNE, J. & LUND, T. 2014 Quantifying Kelvin–Helmholtz instability dynamics observed in noctilucent clouds: 2. Modeling and interpretation of observations. *J. Geophys. Res. Atmos.* **119**, 9359–9375.
- GARANAİK, A. & VENAYAGAMOORTHY, S.K. 2019 On the inference of the state of turbulence and mixing efficiency in stably stratified flows. *J. Fluid Mech.* **867**, 323–333.
- GERZ, T. & SCHUMANN, U. 1996 A possible explanation of countergradient fluxes in homogenous turbulence. *Theor. Comput. Fluid Dyn.* **8**, 169–181.
- GREGG, M.C., D’ASARO, E.A., RILEY, J.J. & KUNZE, E. 2018 Mixing efficiency in the ocean. *Ann. Rev. Mar. Sci.* **10** (1), 443–473.
- HAZEL, P. 1972 Numerical studies of the stability of inviscid stratified shear flows. *J. Fluid Mech.* **51**, 39–61.
- HOWLAND, C.J., TAYLOR, J.R. & CAULFIELD, C.P. 2020 Mixing in forced stratified turbulence and its dependence on large-scale forcing. *J. Fluid Mech.* **898** (A7), 1–27.
- HUSSAIN, F. 1986 Coherent structures and turbulence. *J. Fluid Mech.* **173**, 303–356.
- IVEY, G.N. & IMBERGER, J. 1991 On the nature of turbulence in a stratified fluid. Part I: the energetics of mixing. *J. Phys. Oceanogr.* **21**, 650–658.
- IVEY, G.N., WINTERS, K.B. & KOSEFF, J.R. 2008 Density stratification, turbulence, but how much mixing? *Annu. Rev. Fluid Mech.* **40**, 169–184.
- JAYNE, S. 2009 The impact of abyssal mixing parameterizations in an ocean general circulation model. *J. Phys. Oceanogr.* **39**, 1756–1775.
- KAMINSKI, A.K., CAULFIELD, C.P. & TAYLOR, J.R. 2017 Nonlinear evolution of linear optimal perturbations of strongly stratified shear layers. *J. Fluid Mech.* **825**, 213–244.
- KAMINSKI, A.K. & SMYTH, W.D. 2019 Stratified shear instability in a field of pre-existing turbulence. *J. Fluid Mech.* **862**, 639–658.
- KOMORI, S. & NAGATA, K. 1996 Effect of molecular diffusivities on counter-gradient scalar and momentum transfer in strongly stable stratification. *J. Fluid Mech.* **326**, 205–237.
- MAFFIOLI, A., BRETHEROUWER, G. & LINDBORG, E. 2016 Mixing efficiency in stratified turbulence. *J. Fluid Mech.* **794** (R3), 1–12.
- MASHAYEK, A., CAULFIELD, C. & PELTIER, W. 2017a Role of overturns in optimal mixing in stratified mixing layers. *J. Fluid Mech.* **826**, 522–552.
- MASHAYEK, A., CAULFIELD, C.P. & PELTIER, W.R. 2013 Time-dependent, non-monotonic mixing in stratified turbulent shear flows: implications for oceanographic estimates of buoyancy flux. *J. Fluid Mech.* **736**, 570–593.
- MASHAYEK, A. & PELTIER, W.R. 2012a The ‘zoo’ of secondary instabilities precursory to stratified shear flow transition. Part 1: shear aligned convection, pairing, and braid instabilities. *J. Fluid Mech.* **708**, 5–44.
- MASHAYEK, A. & PELTIER, W.R. 2012b The ‘zoo’ of secondary instabilities precursory to stratified shear flow transition. Part 2: the influence of stratification. *J. Fluid Mech.* **708**, 45–70.
- MASHAYEK, A. & PELTIER, W.R. 2013 Shear-induced mixing in geophysical flows: does the route to turbulence matter to its efficiency? *J. Fluid Mech.* **725**, 216–261.
- MASHAYEK, A., SALEHIPOUR, H., BOUFFARD, C.E., CAULFIELD, C.P., FERRARI, R., NIKURASHIN, M., PELTIER, W.R. & SMYTH, W.D. 2017b Efficiency of turbulent mixing in the abyssal ocean circulation. *Geophys. Res. Lett.* **44**, 6296–6303.
- MATER, B.D. & VENAYAGAMOORTHY, S.K. 2014 A unifying framework for parameterizing stably stratified shear-flow turbulence. *Phys. Fluids* **26** (3), 036601.
- MOSER, R.D. & ROGERS, M.M. 1993 The three-dimensional evolution of a plane mixing layer: pairing and transition to turbulence. *J. Fluid Mech.* **247**, 275–320.
- OSBORN, T.R. 1980 Estimates of the local rate of vertical diffusion from dissipation measurements. *J. Phys. Oceanogr.* **10**, 80–89.
- PHAM, H.T. & SARKAR, S. 2010 Transport and mixing of density in a continuously stratified shear layer. *J. Turbul.* **11**, 1–23.
- PHAM, H.T., SARKAR, S. & BRUCKER, K.A. 2009 Dynamics of a stratified shear layer above a region of uniform stratification. *J. Fluid Mech.* **630**, 191–223.
- PORTWOOD, G.D., DE BRUYN KOPS, S.M. & CAULFIELD, C.P. 2019 Asymptotic dynamics of high dynamic range stratified turbulence. *Phys. Rev. Lett.* **122**, 194504.
- SALEHIPOUR, H. & PELTIER, W.R. 2015 Diapycnal diffusivity, turbulent Prandtl number and mixing efficiency in Boussinesq stratified turbulence. *J. Fluid Mech.* **775**, 464–500.

*Turbulent shear layers in a uniformly stratified background*

- SALEHIPOUR, H., PELTIER, W.R. & MASHAYEK, A. 2015 Turbulent diapycnal mixing in stratified shear flows: the influence of Prandtl number on mixing efficiency and transition at high Reynolds number. *J. Fluid Mech.* **773**, 178–223.
- SALEHIPOUR, H., PELTIER, W.R., WHALEN, C.B. & MACKINNON, J.A. 2016 A new characterization of the turbulent diapycnal diffusivities of mass and momentum in the ocean. *Geophys. Res. Lett.* **43** (7), 3370–3379.
- SCOTTI, A. & WHITE, B. 2014 Diagnosing mixing in stratified turbulent flows with a locally defined available potential energy. *J. Fluid Mech.* **740**, 114–135.
- SHIH, L.H., KOSEFF, J.R., FERZIGER, J.H. & REHMANN, C.R. 2000 Scaling and parameterization of stratified homogeneous turbulent shear flow. *J. Fluid Mech.* **412**, 1–20.
- SHIH, L.H., KOSEFF, J.R., IVEY, G.N. & FERZIGER, J.H. 2005 Parameterization of turbulent fluxes and scales using homogeneous sheared stably stratified turbulence simulations. *J. Fluid Mech.* **525**, 193–214.
- SMYTH, W.D. & MOUM, J.N. 2000 Length scales of turbulence in stably stratified mixing layers. *Phys. Fluids* **12** (6), 1327–1342.
- SMYTH, W.D., MOUM, J.N. & CALDWELL, D.R. 2001 The efficiency of mixing in turbulent patches: inferences from direct simulations and microstructure observations. *J. Phys. Oceanogr.* **31**, 1969–1992.
- SMYTH, W.D., MOUM, J.N. & NASH, J.D. 2011 Narrowband oscillations at the upper equatorial ocean. Part II: properties of shear instabilities. *J. Phys. Oceanogr.* **41**, 412–428.
- STRANG, E.J. & FERNANDO, H.J.S. 2001 Entrainment and mixing in stratified shear flows. *J. Fluid Mech.* **428**, 349–386.
- TAKAMURE, K., ITO, Y., SAKAI, Y., IWANO, K. & HAYASE, T. 2018 Momentum transport process in the quasi self-similar region of free shear mixing layer. *Phys. Fluids* **30**, 015109.
- THORPE, S.A. 2012 On the Kelvin–Helmholtz route to turbulence. *J. Fluid Mech.* **708**, 1–4.
- VANDINE, A., CHONGSIRIPINYO, K. & SARKAR, S. 2018 Hybrid spatially-evolving DNS model of flow past a sphere. *Comput. Fluids* **171**, 41–52.
- VENAYAGAMOORTHY, S.K. & KOSEFF, J.R. 2016 On the flux Richardson number in stably stratified turbulence. *J. Fluid Mech.* **798**, R1.
- WATANABE, T., RILEY, J.J., NAGATA, K., ONISHI, R. & MATSUDA, K. 2018 A localized turbulent mixing layer in a uniformly stratified environment. *J. Fluid Mech.* **849**, 245–276.
- WHALEN, C., MACKINNON, J.A., TALLEY, L. & WATERHOUSE, A.F. 2015 Estimating the mean diapycnal mixing using a finescale strain parameterization. *J. Phys. Oceanogr.* **45**, 1174–1188.
- WINTERS, K.B., LOMBARD, P.N., RILEY, J.J. & D’ASARO, E.A. 1995 Available potential energy and mixing in density-stratified fluids. *J. Fluid Mech.* **289**, 115–128.